Struct Bond (2015) 164: 231–292
DOI: 10.1007/430_2014_155

Published online: 2 October 2014

Spectroscopy Methods for Molecular Nanomagnets

Michael L. Baker, Stephen J. Blundell, Neus Domingo, and Stephen Hill

Abstract This chapter provides a detailed overview of some of the primary spectroscopic methods that have contributed to the current understanding of molecular nanomagnets (MNs). These include: electron paramagnetic resonance (EPR); optical spectroscopy, including magnetic and X-ray magnetic circular dichroism (MCD/XMCD); inelastic neutron scattering (INS); and muon spin rotation (μ^+SR). For each technique, a historical survey of the most important discoveries is provided, up to and including the most recent developments. Each section gives an introduction to the theoretical principles underpinning the techniques, as well as a description of experimental requirements and protocols. A common theme among the described spectroscopies is the fact that state-of-the-art measurements typically have to be performed at major research facilities such as synchrotrons (terahertz EPR and XMCD), high magnetic field laboratories (EPR), and accelerator facilities or reactors (INS and μ^+SR). Details of such facilities are given where appropriate. Forefront issues that are addressed in the chapter include: the fundamental properties of both mono- and poly-nuclear single-molecule magnets (SMMs); the deployment of MNs in quantum information processing applications; the addressing of individual magnetic molecules on surfaces or in devices; the probing of spin dynamics in MNs using EPR, INS, and μ^+SR; and studies of long-range magnetic

M.L. Baker
Department of Physics, City College of New York, CUNY, New York, NY 10031, USA

Department of Physics, New York University, New York, NY 10003, USA

S.J. Blundell
Department of Physics, Clarendon Laboratory, University of Oxford, Oxford OX1 3PU, UK

N. Domingo
Centre d'Investigació en Nanociència i Nanotecnologia (ICN2-CSIC), Campus UAB, 08193 Bellaterra, Spain

S. Hill (✉)
Department of Physics and National High Magnetic Field Laboratory, Florida State University, Tallahassee, FL 32310, USA
e-mail: shill@magnet.fsu.edu

ordering in MN crystals. An extensive list of references is provided. The chapter is intended for physicists, chemists, and materials scientists, particularly junior researchers who are just starting work in the field.

Keywords Electron paramagnetic resonance · Inelastic neutron scattering · Magnetic circular dichroism · Muon spin rotation · X-ray magnetic circular dichroism

Contents

1 Introduction

The chapter begins by introducing electromagnetic/photon probes, starting with a section on electron paramagnetic resonance (EPR – Sect. 2), which was one of the first spectroscopic methods applied to the study of single-molecule magnets (SMMs) [1]. This is followed by a section on surface-sensitive magneto-optical techniques, including magnetic circular dichroism (MCD) and X-ray MCD (XMCD), which have found increased applicability in recent years as researchers have attempted to study the properties of individual molecules grafted onto surfaces (Sect. 3). The last two sections of the chapter switch to local probes that have mass – namely inelastic neutron scattering (INS – Sect. 4) and muon spin rotation (μ^+SR – Sect. 5) spectroscopy. Each of the described techniques offers advantages for studying various types of molecules in different environments. For example, high-field EPR is particularly suited to investigations of anisotropic molecules with large magnetic moments. For this reason, an extensive introduction to the spin-Hamiltonian formalism and the physics of SMMs is given in Sect. 2. Likewise,

INS is highly suited to studies of the collective excitations of spins in antiferromagnetically coupled molecules. Therefore, a more in-depth discussion of such systems is given in Sect. 4. Less detail is devoted to the deposition of molecules onto surfaces because this is discussed in detail elsewhere in this book.

2 Electron Paramagnetic Resonance

EPR and, in particular, high-field EPR (HFEPR [2]) have played a pivotal role in the study of SMMs and other molecule-based magnetic materials. Indeed, one of the very first papers on the prototypical SMM, $[Mn_{12}O_{12}(O_2CCH_3)_{16}(H_2O)_4]\cdot 2CH_3CO_2H\cdot 4H_2O$ ($Mn_{12}Ac$), included continuous-wave (cw) HFEPR data that confirmed the molecular spin $S = 10$ ground state and appreciable magnetic anisotropy [1]. This work was followed by more detailed measurements on both polycrystalline [3] and single-crystal [4] samples, enabling precise elucidation of a set of effective spin Hamiltonian parameters. Likewise, the first report of the magnetic properties of the widely studied Fe_8 SMM included detailed cw HFEPR measurements [5]. During the last decade, pulsed EPR measurements have played an increasingly important role in the study of molecular nanomagnets (MNs), with a view to their potential use in quantum information technologies (see, e.g., [6–10]). This section begins with an introduction and background to the use of cw EPR in the study of SMMs, followed by an extensive survey of the important applications. The section ends with a short review of recent pulsed EPR investigations of MNs.

2.1 Cw HFEPR

The importance of high magnetic fields and high EPR frequencies in the study of SMMs becomes apparent when one examines the simplest effective Hamiltonian describing the spin degrees of freedom of a well isolated orbital singlet ground state associated with a 3*d* transition metal ion [11]. Assuming the symmetry of the local coordination environment allows for such a description, one may introduce magnetic anisotropy by treating the spin-orbit interaction ($\lambda\vec{\mathbf{L}}\cdot\vec{\boldsymbol{s}}$) as a perturbation of the zeroth-order Hamiltonian describing the effects of electrostatic and ligand/crystal-field interactions on the basis of orbital states associated with the 3*d* ion. This procedure enables a description of the lowest orbital singlet in terms of an effective spin-only Hamiltonian (effective because the eigenstates are not pure spin states):

$$\widehat{H} = \mu_B \boldsymbol{B}\cdot\left(g_e\overleftrightarrow{\mathbf{I}} + 2\lambda\overleftrightarrow{\mathbf{\Lambda}}\right)\cdot\hat{\boldsymbol{s}} + \hat{\boldsymbol{s}}\cdot\lambda^2\overleftrightarrow{\mathbf{\Lambda}}\cdot\hat{\boldsymbol{s}}. \quad (1)$$

Here, λ is the spin-orbit coupling constant (which is typically reduced relative to the free-ion value), and $\overleftrightarrow{\mathbf{\Lambda}}$ parameterizes the matrix elements arising from the spin-orbit mixing between excited crystal-field states (at energy ε_i) and the orbital singlet ground state (at energy ε_o); it should be noted that $\overleftrightarrow{\mathbf{\Lambda}}$ contains the energy denominators, $\Delta_i = \varepsilon_i - \varepsilon_o$. The remaining quantities in Eq. (1) include the effective spin operator, $\hat{\boldsymbol{s}}$, the identity matrix, $\overleftrightarrow{\mathbf{I}}$, the free electron Landé g_e-value, and the Bohr-magneton, μ_B. Equation (1) simplifies to the more familiar form [11, 12]:

$$\widehat{H} = \mu_B \boldsymbol{B} \cdot \overleftrightarrow{g} \cdot \hat{\boldsymbol{s}} + \hat{\boldsymbol{s}} \cdot \overleftrightarrow{d} \cdot \hat{\boldsymbol{s}}, \tag{2}$$

where $\overleftrightarrow{g}$ and $\overleftrightarrow{d}$ represent effective Landé and zero-field-splitting (zfs) tensors, respectively; lowercase $\overleftrightarrow{d}$ is employed here to differentiate the single-ion case from the giant spin approximation (GSA) discussed below. The spin multiplicity of the ground state gives rise to $2s+1$ eigenstates that, in the absence of spin-orbit coupling, would be degenerate in zero applied magnetic field. In the typical cw EPR experiment, a swept magnetic field is employed in order to vary the Zeeman energy spacing between m_s spin-projection states. Resonant absorption of microwaves then occurs when the spacing between states connected by the magnetic dipole selection rule ($\delta m_s = \pm 1$) is equal to the microwave energy quantum, hv, resulting in $2s$ distinct EPR transitions. In the isotropic ($\lambda = 0$) case, these transitions would all occur at the same resonance field, $B_{res} = hv/g\mu_B$ ($\equiv 1$ T for a microwave frequency of 28 GHz), i.e., just a single resonance would be observed (neglecting electron-nuclear hyperfine couplings). For the anisotropic case, the second term in Eq. (2) lifts the zero-field degeneracies between states with different absolute m_s values, resulting in a separation of the $2s$ distinct EPR transitions observed in a field-swept single-crystal EPR experiment (see Fig. 1 and discussion below). For a tetragonal crystal-field, the separation between successive EPR peaks is given by $\Delta B_{res} = 2d_{zz}/g\mu_B$, where d_{zz} is the only non-zero (uniaxial) component of the $\overleftrightarrow{d}$ tensor. One thus sees that the more anisotropic the system, the greater the field range [$= (2s-1)\,\Delta B_{res}$] over which the full EPR spectrum extends. Moreover, in order to access many of the EPR transitions, the microwave quantum, hv, must exceed the zfs for cases with $s > ½$. For many transition metal complexes, these constraints require EPR spectrometers that operate over magnetic field and frequency ranges that far exceed those of commercial instruments. Hence, most of the data found in the literature on highly anisotropic molecular magnets have been recorded on home-built spectrometers, many of which are located at major user facilities such as the high magnetic field laboratories in Dresden/Grenoble [14] and Florida [15, 16], or terahertz light sources such as BESSY in Berlin [17].

The magnetic anisotropy discussed above also lies at the heart of SMM physics [12, 18]. Again, considering the uniaxial case with $d_{zz} < 0$ (easy-axis anisotropy), the spin "up" and "down" states with $m_s = \pm s$ lie lowest in energy. Therefore, in

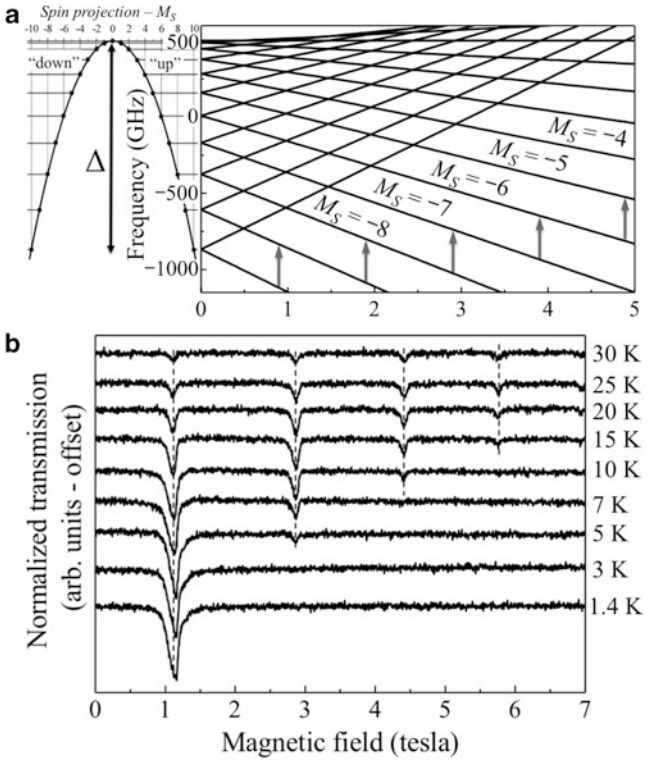

Fig. 1 (**a**) Zeeman diagram generated for spin $S = 10$ according to a purely second-order giant spin Hamiltonian, with $D = -0.66$ K, $E = 0$, and $H//z$. The eigenstates are plotted versus the spin projection, M_S, on the left to make a connection to the parabolic energy barrier (Δ) separating spin-up and down states. Several possible EPR transitions are marked by *vertical gray arrows* in the main panel. (**b**) Temperature dependence of the easy-axis ($H//c$) HFEPR spectra for $Mn_{12}Bu^tAc$ at a frequency of 336 GHz. Adapted with permission from [13]. Copyright 2013 American Chemical Society

order for an "up" spin to reverse its orientation, it must overcome an energy barrier created by the higher-lying intervening spin projection states with $|m_s| < s$. However, in nearly all cases [19], quantum fluctuations (through barrier tunneling) prevent complete blocking of the magnetic moment associated with a single 3*d* ion. For this reason, all of the early work on SMMs involved large, polynuclear transition metal clusters with giant ferro- or ferrimagnetically coupled spin ground states. The stabilization of a giant (~mesoscopic) spin moment suppresses quantum fluctuations, leading to the situation in which the $20\mu_B$ magnetic moment associated with the $S = 10$ $Mn_{12}Ac$ SMM completely blocks below ~4 K [1, 20, 21]. A full treatment of the exchange coupling between twelve anisotropic spins is computationally challenging [20]. However, in many SMMs (including Mn_{12} and Fe_8), these couplings are sufficiently strong that one may approximate the low-energy/low-temperature physics by assuming the spins to be rigidly coupled, giving rise to an effective molecular giant spin, *S*, ground state [3, 12].

The GSA allows for a description of the low-energy magnetic spectrum of a SMM using the Hamiltonian of Eq. (2), albeit with the single-ion spin operator, $\hat{\boldsymbol{s}}$, replaced by a corresponding giant spin operator, $\hat{\boldsymbol{S}}$ [12]. One can diagonalize (rotate) and renormalize the molecular $\overleftrightarrow{\boldsymbol{D}}$ tensor such that the second-order zfs is expressed in terms of just two parameters: the well known axial and rhombic anisotropy parameters D and E, respectively. When written in this form, the second term in Eq. (2) becomes $D\hat{S}_z^2 + E\left(\hat{S}_x^2 - \hat{S}_y^2\right)$. Figure 1a shows the Zeeman energy level diagram obtained using the above Hamiltonian for an easy-axis ($D < 0$) $S = 10$ system such as $Mn_{12}Ac$ (with E set to zero), with the magnetic field applied parallel to the easy-axis. The zero-field spectrum is shown to the left of the Zeeman diagram, illustrating the potential energy barrier ($\Delta = DS^2$) separating spin "up" and "down" states; the D ($= -0.66$ K) parameter employed for Fig. 1a was chosen to approximately mimic the $Mn_{12}Ac$ SMM [22] (note – 1,000 GHz $\equiv$ 48 K $\equiv$ 33.3 cm^{-1}). The first thing to note is the ~300 GHz zero-field separation between the $M_S = \pm 10$ and ± 9 states. Frequencies in excess this zfs are therefore required in order to excite EPR transitions from the lowest-lying $M_S = -10$ Zeeman level. A single-crystal EPR experiment performed in the high-field/frequency limit would result in $2S$ ($= 20$ for $Mn_{12}Ac$) evenly spaced easy-axis resonances, with a spacing given by $\Delta B_{res} = 2D/g\mu_B \approx D/\mu_B \approx 1$ T for the D parameter employed in Fig. 1a; representative transitions responsible for such resonances are indicated by vertical gray arrows in Fig. 1a.

Figure 1b shows actual 336.3 GHz absorption mode EPR spectra obtained for a single-crystal sample of the high-symmetry $[Mn_{12}O_{12}(O_2CCH_2Bu^t)_{16}(CH_3OH)_4]\cdot CH_3OH$ ($Mn_{12}Bu^tAc$) SMM, with the magnetic field applied parallel to its magnetic easy-axis [13, 22–26]. The first thing to note is the uneven spacing between EPR transitions, and the fact that these spacings significantly exceed the $\Delta B_{res} \approx 1$ T predicted above ($Mn_{12}Ac$ and $Mn_{12}Bu^tAc$ have virtually identical Hamiltonian parameters [22]). These observations immediately highlight limitations of the second-order perturbative Hamiltonian of Eq. (2). First and foremost, the second-order zfs Hamiltonian possesses rigorous D_{2h} symmetry (or $D_{\infty h}$ when $E = 0$) [12], which is incompatible with the local S_4 point group ($I\overline{4}$ space group) symmetry appropriate to many Mn_{12} SMMs [18, 22]. In particular, E is strictly forbidden for $Mn_{12}Bu^tAc$, and it is clear that a single D parameter cannot account for the uneven spacing of the EPR transitions seen in Fig. 1b. It was recognized early on [3, 4] that one could simulate the HFEPR spectra of $Mn_{12}Ac$ using extended Stevens operators to account for the zfs interactions [12], i.e.,

$$\hat{H}_{zfs} = \sum_{p}^{2S} \sum_{q=0}^{p} B_p^q \hat{O}_p^q, \tag{3}$$

where $\hat{O}_p^q\left(\hat{S}_x, \hat{S}_y, \hat{S}_z\right)$ represent the operators [27, 28], and B_p^q the associated phenomenological (or effective) zfs parameters. The subscript p denotes the order

of the operator, which must be even because of the time reversal invariance of the spin-orbit interaction; the order is also limited by the total spin of the molecule ($p \leq 2S$). The superscript q ($\leq p$) denotes the rotational symmetry of the operator about the quantization (z-) axis. The summation in Eq. (3) includes the second-order axial anisotropy with $D = 3B_2^0$ and $E = B_2^2$; therefore, the more general GSA Hamiltonian is obtained by replacing the last term in Eq. (2) by $\hat{H}_{\text{zfs}}$.

Use of extended Stevens operators enables application of the effective spin Hamiltonian formalism to almost any SMM, as well as many other MNs, irrespective of symmetry or spin state. A drawback of this approach is the fact that it can be challenging to relate the obtained phenomenological B_p^q parameters to the microscopic structural details of the molecule under investigation; we come back to this issue further below. Nevertheless, the GSA has proven remarkably successful in terms of explaining many low-temperature magnetic properties of SMMs, including spectacular effects due to quantum tunneling and quantum interference, as seen in magnetization hysteresis measurements [12]. HFEPR has played an essential role in understanding these phenomena by providing direct access to an underlying spin Hamiltonian (in this case the GSA). In fact, at a very basic level, quantum tunneling of magnetization (QTM [29, 30]) measurements can be thought of as a zero-frequency EPR experiment given that hysteresis loop steps are observed at the level-crossings seen in Fig. 1a [separated by $\Delta B_{\text{QTM}} \approx D/g\mu_B \approx 0.5$ T]. Thus, one can extract D and higher-order ($p > 2$) diagonal ($q = 0$) terms from the locations of magnetization steps seen in hysteresis loop measurements performed with the field applied parallel to the magnetic easy-axis [12]. Meanwhile, off-diagonal ($q \neq 0$, tunneling) terms can, in principle, be deduced from QTM rates and quantum interference measurements [31]. However, such studies have only been performed for a handful of SMMs to date, primarily because of the need to employ specialized high-sensitivity magnetometers (micro-SQUID [31] or micro-Hall [32]), and because experiments must be performed well below the blocking temperature (typically $\ll 1$ K) using dilution refrigerators.

A drawback of the magnetic measurements described above is that hysteresis loop steps occur at field locations that depend both on the field-independent interactions, $\hat{H}_{\text{zfs}}$, and the field-dependent Zeeman interaction. Thus, it can be difficult to simultaneously constrain both the g tensor and zfs parameters. This is where HFEPR becomes extremely powerful. By performing measurements at multiple high-frequencies, one can independently constrain the field-dependent (Zeeman) and field-independent (zfs) interactions [32]. For a uniaxial SMM, application of a field parallel to z (easy-axis) ensures that the Zeeman interaction appears on the diagonal of the spin Hamiltonian. The effects of the off-diagonal ($q \neq 0$) zfs interactions are negligible in this situation because the EPR spectrum is dominated by the lowest-lying Zeeman levels ($M_S = -10, -9, -8\ldots$), and these are mostly protected from each other, i.e., they do not cross. Even those low-lying states that do cross (e.g., $M_S = +10$ and -9, $M_S = +10$ and -8) are largely immune to the off-diagonal terms because of the enormous differences in spin projection: the symmetry-allowed $\hat{O}_4^4 \equiv \frac{1}{2}\left(\hat{S}_+^4 + \hat{S}_-^4\right)$ interaction connects $M_S = +10$ and -6

($\Delta M_S = 16$) only as a fourth-order perturbation; this is the reason why the quantum relaxation is so slow at these (avoided) level crossings, i.e., the tunneling rates (gaps) are incredibly small (~Hz for the first few resonances for Mn_{12}). Consequently, the easy-axis HFEPR peak positions vary linearly with applied field, as seen in Fig. 2a, which plots multi-frequency single-crystal data for $Mn_{12}Bu^tAc$ [26]. Fits to these data yield g_z, D, B_4^0 and, in principle, higher order $q = 0$ terms; g_z is constrained by the slope of the lines through the data points, while the remaining parameters dictate the field-independent spacings between the data points. Because these measurements are spectroscopic, they provide extremely tight constraints on the axial zfs parameters. As such the obtained values are far more reliable than those deduced from thermodynamic measurements (magnetization, susceptibility, etc.) that yield data sets with relatively little information content.

The remaining off-diagonal ($q \neq 0$) terms are obtained by applying a large magnetic field transverse to the easy axis. In this situation, the now dominant Zeeman interaction dictates the quantization axis so that previously off-diagonal terms appear along the diagonal of the spin Hamiltonian [32]. The components of the g- and zfs tensors can then be picked off by applying a magnetic field along different axes of a single crystal – see Fig. 2. In practice, such experiments are extremely challenging and time consuming, requiring a cavity (for sensitivity to small crystals) and two-axis rotation capabilities. Consequently, only a few such examples involving SMMs can be found in the literature [23, 32–40]. A more direct approach involves studying a finely ground powder sample. In this situation, all crystal orientations contribute equally to the EPR absorption (provided the powder is constrained). By recording the spectrum in derivative mode (using field modulation), features emerge that correspond to the turning points in the full two-axis, angle-dependent EPR spectrum, i.e., the hard, intermediate, and easy directions, corresponding to x, y, and z for a rhombic system. Example powder HFEPR spectra are displayed in Fig. 3 for the biaxial Fe_8 SMM [5], illustrating good separation of the x, y, and z components. However, powder measurements typically require a lot of sample (>50 mg) because the EPR absorption now extends over the entire spectrum [$\Delta B_{spec} = 2D\ (2S-1)/g\mu_B$], as opposed to being concentrated within just a few sharp resonances. Moreover, the act of making a powder can affect sample quality, particularly in cases involving volatile lattice solvent molecules (discussed below [41]). Lastly, one does not know a priori where the turning points in the spectrum should occur, thus making it difficult to know exactly which zfs interactions contribute to the anisotropy in the hard plane of a SMM [32]. One can, in principle, invoke symmetry arguments to eliminate certain possibilities. But this does not always work for low-symmetry crystals.

Using microwave resonators, HFEPR studies of very small (~0.1 mm^3 or ~100 μg) single-crystal samples of high quality become feasible [16]. Field rotation studies then provide direct information on the symmetries of the dominant transverse zfs operators, as illustrated by the data in Fig. 2c for $Mn_{12}Ac$ [34]. In this case, the HFEPR spectrum consists of several contributions due to the existence of multiple species of Mn_{12} molecule possessing different zfs parameters.

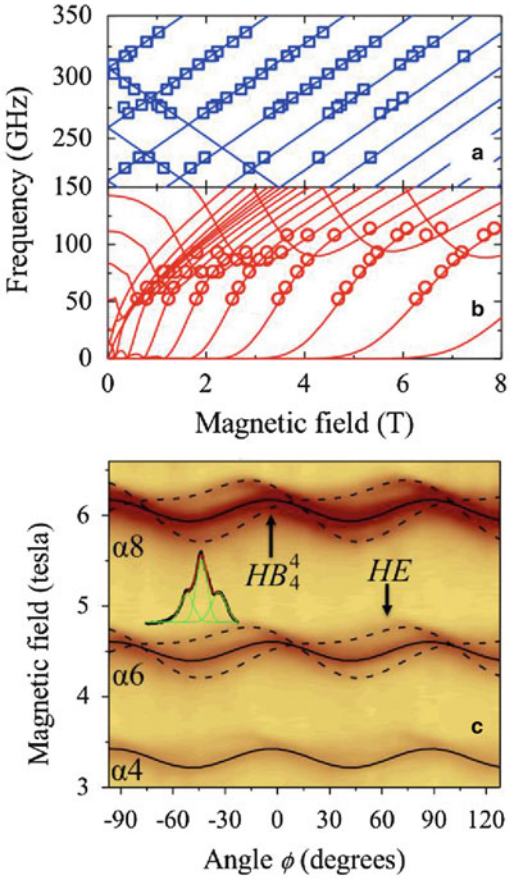

Fig. 2 (**a**) Fits to the frequency dependence of easy-axis HFEPR peak positions for a $Mn_{12}Bu^tAc$ single-crystal (see Fig. 1b and [24]); (**b**) corresponding fits to the hard-plane peak positions. The easy-axis data constrain the axial (*z*-) components of the spin Hamiltonian, while the hard-plane data constrain the transverse components (see main text). (**c**) 2D contour plot of the $T = 15$ K HFEPR absorption intensity versus magnetic field strength and its orientation, ϕ, within the hard (*xy*-) plane for a deuterated d-$Mn_{12}Ac$ single-crystal (from [24]). The *darker shades* correspond to stronger absorption and the resonances have been labeled according to the scheme described in [33]. Each resonance consists of multiple components (see *inset*): the central peak exhibits pure fourfold symmetry, whereas the low- and high-field shoulders exhibit a superposition of two and fourfold behavior. Fits to the central peak (*solid lines*) and the shoulders (*dashed lines*) are superimposed on the plot, and the approximate orientations of the hard-axes associated with the intrinsic B_4^4 (HB_4^4) and extrinsic E (HE) interactions are indicated. Adapted with permission from [24]. Copyright 2005 Elsevier

The dominant central portion of the spectrum (due to ~50% of the molecules) exhibits a fourfold rotational symmetry, with turning points separated by 45° [not the 90° expected on the basis of the second order rhombic Hamiltonian of Eq. (2)]. One would not know this from a powder measurement, although symmetry

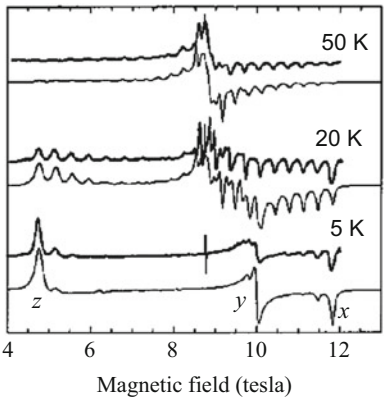

Fig. 3 Powder HFEPR spectra of the Fe_8 SMM at 245 GHz at the three indicated temperatures. The *upper curve* for each temperature corresponds to the experimental spectrum, while the *lower curve* is the simulated spectrum The x, y, and z components of the spectrum are labeled. Adapted with permission from [5]. Copyright 1996 EDP Sciences

considerations suggest that the dominant transverse zfs interactions should posses fourfold symmetry. Closer inspection of the edges of the spectrum reveals satellite peaks that exhibit a superposition of four and twofold rotation patterns [33]. There are two such components (each corresponding to ~25% of the molecules) shifted by 90° so that the summed spectrum retains overall fourfold symmetry. Therefore, roughly 50% of the molecules in a $Mn_{12}Ac$ crystal experience a significant rhombic zfs interaction: 25% with $E > 0$ and 25% with $E < 0$, so that the average rhombicity (symmetry) is zero (fourfold). Here, one sees the remarkable detail that one can obtain from such a spectroscopic measurement; there is no way this amount of information could be extracted from thermodynamic studies. The findings have been correlated both with structural studies [42], INS [43] and magnetic hysteresis measurements in which the rhombic interaction is found to influence the quantum relaxation behavior [44]. The rhombicity is attributed to a discrete disorder associated with an acetic acid solvent molecule that directly influences the coordination (and hence the Jahn-Teller distortion) at one of the Mn^{III} sites. Further details of this solvent induced disorder are given in the following section and can be found in [32–34, 42, 43].

2.2 *Applications of cw EPR*

In spite of the need for very high EPR frequencies (>300 GHz, or >3× the highest frequency available at the time commercially), the Mn_{12} family of SMMs has attracted by far the most interest up to now. There are many reasons for this, foremost among them being the fact that $Mn_{12}Ac$ was the first SMM, boasting the highest blocking temperature until just a few years ago. Indeed, $Mn_{12}Ac$ has sometimes been used as a model system for demonstrating the efficacy of newly developed terahertz spectrometers [17, 45] and EPR techniques [46, 47]. Meanwhile, $Mn_{12}Ac$ has presented many mysteries as well. For example, a complete microscopic understanding of resonant QTM rates remains elusive [12]. The S_4

symmetry of the idealized $Mn_{12}O_{12}$ core is so close to being cylindrical that one expects the quantum tunneling at most of the level crossings (QTM resonances) in Fig. 1 to be strictly forbidden. The reason for this can be traced back to the second order effective single-ion spin Hamiltonian of Eq. (2). When one projects the collective single-ion anisotropies onto the molecular spin $S = 10$ ground state, the transverse component of the second order molecular anisotropy $E\left(\hat{S}_x^2 - \hat{S}_y^2\right)$ exactly cancels [12], i.e., E is strictly forbidden on symmetry grounds (one can think of this as a vector addition in which the transverse components exactly sum to zero). Consequently, QTM would be strictly forbidden in all resonances for an ideal Mn_{12} molecule if the second order Hamiltonian told the entire story. As discussed below, there are several mechanisms that can give rise to higher order transverse anisotropies in the molecular Hamiltonian [Eq. (3)] that are compatible with S_4 symmetry, e.g., $B_4^4 O_4^4 \equiv \frac{1}{2} B_4^4 \left(\hat{S}_+^4 + \hat{S}_-^4\right)$. Nevertheless, these terms are quite weak, and they cannot explain the fact that QTM is observed at all resonances in Fig. 1. However, it does not require much of a distortion to the ideal molecular symmetry to result in a rapid re-emergence (non-cancelation) of the second-order transverse anisotropy, which can dramatically accelerate QTM rates. Therefore, many theoretical and experimental studies have focused on the role of disorder and other factors that influence the QTM relaxation in Mn_{12} SMMs [12, 13, 18, 22–26, 32–34, 42–62].

Perhaps the best illustration of the influence of disorder in SMM crystals involves an early curiosity associated with $Mn_{12}Ac$. It had been recognized since some of the first investigations that roughly 5–8% of the sample relaxes much faster than the canonical high-symmetry Mn_{12} species [63]. The faster relaxing molecules are found in all samples and are believed to be randomly distributed throughout the crystal [48, 64]. They can be detected either from AC susceptibility measurements, where they give rise to a small out-of-phase peak at temperatures well below that of the main species [26], or in low-temperature hysteresis studies where they relax at much lower fields than the main species [48]. Detailed synthetic work, involving ligand substitution and crystallization from a variety of solvents, resulted in the discovery of many different forms of Mn_{12} possessing the same neutral $Mn_{12}O_{12}$ core (see, e.g., [13, 22, 26, 38, 53, 65, 66], or [67] for a comprehensive review). These Mn_{12} complexes can be grouped broadly into two categories [38, 67]: (1) fast-relaxing (FR) and (2) slow relaxing (SR). Indeed, a histogram of the effective magnetization relaxation barriers (deduced from frequency-dependent AC susceptibility measurements), for around 20 different Mn_{12} complexes, reveals a bimodal distribution ([48] and Hendrickson, private communication) with values in the 25–45 K range for the FR species and the 60–80 K range for the SR species. In many of the cases where the FR species was obtained in single-crystal form, it was found that one or more of the Jahn-Teller elongation axes associated with the Mn^{III} atoms was abnormally oriented [38, 53, 65] in comparison to the usual SR form [1, 13, 22, 26], thereby significantly lowering the symmetry of the Mn_{12} core.

Single-crystal HFEPR studies provided crucial insights into the reduced relaxation barrier associated with the FR form of Mn_{12}, and the importance of lattice

solvent molecules [38]. Measurements were performed on a low-symmetry version of the $Mn_{12}Bu^tAc$ molecule (that co-crystallizes with $CH_2Cl_2/MeNO_2$ solvents [65]) in which the Jahn-Teller distortion associated with one of the Mn^{III} atoms has flipped so that it is close to parallel to the plane of the molecule, in contrast to the other seven which are roughly perpendicular to this plane. HFEPR studies revealed only a moderate (~10%) reduction in the molecular D parameter. However, a very significant molecular E value (~D/6) was found [38]. In other words, the axial anisotropy is only moderately reduced as a result of re-orienting the local anisotropy at one of the eight Mn^{III} sites. The very significant second-order rhombic molecular anisotropy emerges due to non-cancelation of the transverse components of the single-ion anisotropies. In this case, it is the transverse projection of the axial anisotropy (d) associated with the abnormally oriented Jahn-Teller axis that gives rise to the large molecular E value. In turn, this causes very strong mixing of (or tunneling between) M_S states well below the top of the barrier generated purely on the basis of the axial $D\hat{S}_z^2$ term (see Fig. 1a) [38]. Thus, spins can relax via states well below the top of the classical barrier, explaining the observed fast relaxation behavior. The HFEPR studies were extremely challenging due to the low symmetry structure and because the crystals rapidly lose solvent, leading to a loss of crystallinity. In fact, AC susceptibility studies show that the loss of volatile $CH_2Cl_2/MeNO_2$ solvent leads to a conversion of the FR species into the SR form, and subsequent recrystallization of the dried product from a CH_2Cl_2/MeCN mixture gives good crystals of the pure SR form [65]. Putting everything together, one clearly sees here the dramatic influence of the solvent and subtle crystal packing forces on the quantum properties of SMMs.

The quantum properties of the SR $Mn_{12}Ac$ species are also influenced by an intrinsic disorder associated with the co-crystallizing acetic acid solvent [32]. In fact, this disorder was recognized early on from EPR line-width studies that suggested significant strains (distributions) in the molecular D parameters for both the Fe_8 and $Mn_{12}Ac$ SMMs ($\sigma_D \sim 0.01 - 0.02D$) [45, 49–52]. However, the importance of the disordered solvent was made on the basis of combined X-ray and powder HFEPR studies [42]. The acetic acid forms a hydrogen-bond to the $Mn_{12}O_{12}$ core, resulting in a distortion of the coordination environment around one of the eight Mn^{III} atoms. Although each solvent molecule occupies a position between adjacent Mn_{12} molecules, it can hydrogen-bond to only one of them, resulting in a statistical distribution of solvent isomers with either 0, 1, 2, 3, or 4 hydrogen bonding interactions to the acetic acid. A small fraction of these isomers maintain S_4 symmetry, while the remainder adopt a lower symmetry. Ligand-field calculations show that the low-symmetry isomers acquire non-negligible molecular E values, again due to imperfect cancelation of the transverse components of the second-order single-ion anisotropies [42]. However, the Jahn-Teller axes remain approximately parallel, so the effect is far weaker than the case of the FR Mn_{12} species. Consequently, the influence of the disorder on the QTM relaxation is subtle, albeit measurable [32, 44]. Meanwhile, the solvent isomerism is very apparent in angle-dependent single-crystal HFEPR measurements (a subset of

these data are displayed in Fig. 2c [32–34]). In particular, it is found that the low-symmetry isomers have their easy-axes tilted slightly away from the average crystallographic S_4 (c-) axis; the half-width of the distribution is less than 1° [18, 33], illustrating the remarkable resolution of the EPR technique. Moreover, the tilting and rhombicity (see Fig. 2c) are correlated, as expected on the basis of the solvent isomer model [42].

The original $Mn_{12}Ac$ can be modified to obtain new high-symmetry Mn_{12} SMMs [13, 22–26]. Approaches include substitution of the acetate ligand with bulkier ones such as $BrCH_2CO_2^-$ (BrAc [23, 26]), or $Bu^tCH_2CO_2^-$ (Bu^tAc [13, 24, 25]); water molecules may also be exchanged with alcohols [22]. These modifications primarily influence the environment of the $Mn_{12}O_{12}$ molecule, without affecting internal couplings. Therefore, the $S = 10$ ground state is retained. To date, three new high-symmetry Mn_{12}s have been synthesized and interrogated by HFEPR. They include: $[Mn_{12}O_{12}(O_2CCH_2Br)_{16}(H_2O)_4]\cdot 4CH_2Cl_2$ ($Mn_{12}BrAc$ [23–26]), $[Mn_{12}O_{12}(O_2CCH_2Bu^t)_{16}(MeOH)_4]\cdot CH_3OH$ ($Mn_{12}Bu^tAc$ [13, 24, 25]), and $[Mn_{12}O_{12}(O_2CCH_3)_{16}(CH_3OH)_4]\cdot CH_3OH$ [$Mn_{12}Ac/CH_3OH$] [22]. The latter compound is essentially identical to the original $Mn_{12}Ac$ except that the acetic acid solvent is replaced by methanol. All three complexes possess fourfold symmetric crystal structures ($I4_1/a$ for the BrAc and $I\bar{4}$ for the other two). In the latter two compounds, both the Mn_{12} molecule and the single CH_3OH solvent reside on $I\bar{4}$ (S_4) axes and, although the solvent is disordered, it resides far from the Mn_{12} core [13, 18, 22]. Consequently, hydrogen bonding interactions of the kind found in the original $Mn_{12}Ac$ are absent. The situation in the BrAc complex is slightly different [26]. There are hydrogen bonding interactions between solvents and the Mn_{12} core. However, because of the 4:1 ratio of CH_2Cl_2 and Mn_{12}, these interactions do not perturb the S_4 symmetry of the core. Nevertheless, the CH_2Cl_2 solvent is quite volatile.

Careful studies of the three newer high-symmetry Mn_{12} complexes reveal remarkably clean HFEPR spectra, with absolutely no evidence for the solvent isomerism/disorder found in the original $Mn_{12}Ac$ [13, 22–26]. Angle-dependent single-crystal HFEPR spectra for the $Mn_{12}Bu^tAc$ complex exhibit the ideal fourfold behavior expected on the basis of the intrinsic S_4 symmetry of the $Mn_{12}O_{12}$ core [13, 24, 39]. However, measurements performed on the BrAc complex show a considerable degradation of the EPR spectra when the samples are exposed to air for an extended period [18, 22, 26]. This exposure (or, more precisely, removal from the mother liquid) results in a loss of the volatile CH_2Cl_2 solvent from the lattice. Over time, the HFEPR spectra start to resemble those of the original $Mn_{12}Ac$, with simulations suggesting that the solvent loss generates a similar orientational disorder. Moreover, comparisons of QTM measurements performed on pristine and dried samples reveal remarkable differences [26, 68], once again demonstrating that solvent disorder has a profound influence on the QTM dynamics of high-symmetry SMMs. Similar investigations for a Mn_{12} benzoate complex involving combined magnetic and frequency domain magnetic resonance (FDMR [69] – EPR performed in the frequency domain) measurements concluded that

disorder did not influence the QTM relaxation [57]. However, the Mn_{12} benzoate complex possesses a low symmetry structure to begin with, i.e., it belongs to the FR species [67]. Therefore, it would require an inordinate degree of disorder to accelerate the QTM relaxation beyond the rate dictated by the intrinsic second-order transverse anisotropy. In a related study, it was argued that differences in relaxation found for $Mn_{12}Ac$ and $Mn_{12}Bu^tAc$ are due to differences in dipolar field distributions [62], which are known to play a role in mediating the collective quantum dynamics in SMM crystals [70]. However, this study ignored the documented disorder in $Mn_{12}Ac$ [42]. Instead, comparisons between $Mn_{12}Ac$ and $Mn_{12}Ac/CH_3OH$ allow for an unbiased assessment of this controversy because they have the same structures and, hence, the same dipolar field distributions [12]. HFEPR studies reveal essentially identical axial anisotropy parameters (D and B_4^0), within the experimental uncertainty. Meanwhile, the measured effective relaxation barrier is measurably lower for $Mn_{12}Ac$, demonstrating that the intrinsic solvent disorder increases QTM (M_S state mixing) and promotes under-barrier relaxation [22].

Comparisons of EPR spectra obtained across families of closely related compounds (e.g., Ni_4, Mn_3, and Mn_4) demonstrate that the solvent-free complexes (when they exist) consistently exhibit much sharper spectral features [12, 41, 71]. Stated differently, solvent-containing compounds tend to suffer from disorder that causes significant inhomogeneous broadening (D, E, etc., strain) of the EPR spectra; in some cases, the differences in EPR line-widths can be a factor of 10 between the solvent-containing and solvent-free members of a family that otherwise possess identical molecular cores and identical axial anisotropy parameters [41]. It is assumed that the disorder is related primarily to the loss of solvent from the lattice, although the solvent molecules themselves can be disordered as well. Samples containing more volatile solvents tend to display more disorder [26, 72]. It is therefore not surprising that combined HFEPR and QTM investigations of solvent-free SMMs have revealed important new insights into the physics of SMMs [12, 73–79]. Foremost among these is the clear observation of QTM selection rules dictated by the intrinsic C_3 symmetry of a triangular Mn_3 SMM [75].

In comparison to other bulk low-energy spectroscopic probes (e.g., INS and FDMR), cw HFEPR offers exceptional sensitivity and energy resolution. Indeed, the instrument resolution is limited primarily by the specifications of the magnet (<10 ppm is achievable [80]). The true resolution is therefore usually limited by sample quality. The availability of solvent-free crystals combined with the high resolution of EPR has thus enabled many detailed studies (beyond those described so far) that have made important contributions to the current understanding of MNs. Several such studies have focused on the origin of higher order ($p > 2$) terms in the GSA (Eq. (3) [12, 35, 37, 39, 40, 71, 74–78, 81]). Ligand-field calculations based on non-perturbative methods are known to generate fourth order corrections to Eq. (2) [82], and these terms can in principle survive when projected onto the ground spin state of a multinuclear SMM. However, single-ion zfs interactions of order greater than 2 are strictly forbidden for a spin $s = 1$ ion such as Ni^{II} due to the limited

dimension (3×3) of the Hamiltonian matrix. The S_4-symmetric solvent-free $[Ni(hmp)(dmb)Cl]_4$ (Ni_4) cluster therefore serves as an interesting case study, given that single-crystal HFEPR studies similar to those presented in Fig. 2 reveal significant fourth-order GSA parameters (both B_4^0 and B_4^4) associated with the $S = 4$ ground state [35–37]. Due to the relatively small size of this molecule one can employ a microscopic Hamiltonian that separately takes into account the local spin-orbit anisotropy at each Ni^{II} site, together with the exchange coupling between the ions [74]:

$$\widehat{H} = \sum_{i=1}^{4} \left(\mu_B \boldsymbol{B} \cdot \overleftrightarrow{g}_i \cdot \hat{\boldsymbol{s}}_i + \hat{\boldsymbol{s}}_i \cdot \overleftrightarrow{d}_i \cdot \hat{\boldsymbol{s}}_i \right) + \sum_{i<j}^{4} \hat{\boldsymbol{s}}_i \cdot \overleftrightarrow{J}_{ij} \cdot \hat{\boldsymbol{s}}_j. \tag{4}$$

As can be seen from comparisons with Eq. (2), the first summation accounts for the second-order local anisotropy and Zeeman interaction at the four Ni^{II} sites (labeled by the index i). The second summation parameterizes the exchange interactions between spins i and j. Equation (4) perfectly reproduces the single-crystal HFEPR data for Ni_4, including the uneven easy-axis peak spacings (attributed to B_4^0 within the GSA description), and the fourfold symmetry obtained from angle-dependent measurements (attributed to B_4^4 within the GSA) [35–37]. Moreover, independent HFEPR measurements of the $\overleftrightarrow{d}_i$ tensors, including their orientations, was made possible by studying a solid solution sample of $[Ni_xZn_{1-x}(hmp)(dmb)Cl]_4$ ($x = 0.02$) [83]. Therefore, the only adjustable parameter in the fits to the HFEPR data was the exchange coupling constant, J, which was assumed to be isotropic and the same for all contacts. In other words, the apparent fourth order anisotropy is connected with the exchange coupling within the cluster.

As noted previously, one can determine the second-order anisotropy for a coupled spin system via a procedure that involves projecting the individual second-order anisotropies onto the molecular spin state [74, 84]. However, this procedure is only exact as long as the molecular spin quantum number is exact. If the exchange coupling within a molecule is weak, excited spin states will mix with the ground state. In such situations, the projection method is approximate. One still expects the second-order transverse components to cancel for situations in which the molecular symmetry forbids a rhombic anisotropy, e.g., tetragonal Mn_{12} and Ni_4, or trigonal Mn_3 [12]. However, the transverse components can emerge at higher orders in these situations via the mixing with excited states. By performing a numerical mapping between the parameters employed in the two models [Eqs. (3) and (4)], one finds that the higher order GSA terms scale as inverse powers of the exchange coupling, i.e., $|J|^{-n}$, where $2n = p - 2$ [74, 77]. In essence, the interaction (mixing) between spin multiplets renormalizes the energies within each multiplet. The extent of the mixing depends on the proximity of excited spin states. The renormalization is then captured by adding higher order terms to the GSA Hamiltonian: fourth-order terms arise through first-order mixing, with the energy denominator given by the appropriate multiplet spacing, which is proportional to J, i.e.,

$B_4^4 \propto |J|^{-1}$; sixth-order terms arise through second-order mixing, i.e., $B_6^6 \propto |J|^{-2}$, and so on [12, 77]. These ideas have been beautifully verified through detailed HFEPR studies on Ni_4 [35–37], Fe_3Cr [40], Mn_3 [73–77], Mn_4 [78, 79], a $Mn_{3\times3}$ grid [81], and even Mn_{12} [38]. Importantly, these findings demonstrate that EPR can provide detailed information about the exchange interactions within a SMM, something that was previously thought to be possible only via INS. The magnetic dipole selection rules forbid inter-spin-state transitions. However, the aforementioned spin-state mixing provides indirect access to the exchange physics, and inter-spin transitions can even become allowed in situations where the mixing is strong [81, 85, 86]. Another important conclusion concerns situations with little or no symmetry, where it is clear that any of the terms in Eq. (3) can exist [77]. This has important implications for QTM selection rules, suggesting that disorder can cause tunneling in any resonance, thereby perhaps explaining why intrinsic symmetry enforced QTM selections rules were only observed recently in a solvent free SMM [12, 87]. On the flip side, these investigations demonstrate that one should in principle be able to completely switch off quantum tunneling in high symmetry SMMs if strong enough exchange coupling can be achieved, because all of the symmetry allowed transverse GSA interactions scale as $|J|^{-n}$.

Until fairly recently, most SMM research was directed towards polynuclear 3*d* transition metal clusters, with the synthetic goal of maximizing both the molecular spin state and the cluster anisotropy [88, 89]. However, a number of factors have limited progress based on this strategy, with the record blocking temperature for a Mn_6 cluster [88] only just surpassing that of the original Mn_{12} SMM [1]. Limiting factors include: (1) a tendency for exchange interactions to be both weak (few cm^{-1}) and often antiferromagnetic; (2) the fact that orbital momentum is usually quenched, thus significantly suppressing the magnetic anisotropy; and (3) the difficulties associated with maximally projecting any remaining (second order spin-orbit) axial anisotropy onto the ground spin state of a SMM. HFEPR studies have addressed the latter issue by focusing on families of closely related Mn_3 and Mn_6 SMMs [76, 84, 90, 91], where the Mn_6 molecule can be thought of as a ferromagnetically coupled $[Mn_3]_2$ dimer. A particular attraction is the fact that one can switch the sign of the exchange within the triangular $[Mn^{III}]_3$ units, thereby achieving both high-spin ($S = 6$) and low-spin ($S \lesssim 2$) states (or $S = 12$ and $S = 4$ states in the case of Mn_6). Extensive studies of spin states ranging from $S = 4$ to 12 (also including Mn_{12}) reveal experimental anisotropy barriers that vary by no more than a factor of 2 [76], in spite of the fact that the Jahn-Teller axes on the Mn^{III} ions are reasonably parallel in all cases. The reason for this is again related to the projection of the single-ion anisotropies onto the molecular spin ground state. The molecular *D* value is given by a weighted sum of the anisotropies of the constituent ions (d_i), where the weighting is inversely proportional to the total molecular spin, *S* [84, 92]. Thus, *D* decreases as *S* increases. If all spins are coupled ferromagnetically and their $\overleftrightarrow{d}$ tensors parallel, the theoretical best that one can hope to achieve is a molecular barrier ($\sim DS^2$) that scales linearly with *S* or *N* (the number of spins in the molecule) [76]. Experiments comparing Mn_3 ($S = 6$) and Mn_6 ($S = 12$)

broadly agree with this rule, even though it is exact only in the large N limit. The situation is worse when comparing low-spin and high-spin molecules, where theory predicts a weaker dependence of the barrier on S [84], i.e., the barrier is almost S independent [92]. Again, this is borne out by experiment [76]. Therefore, it is no surprise that the optimum $[Mn^{III}]_N$ SMM has a nuclearity of just six [89]!

Given the above situation, it has become clear that the more direct route to SMMs that can be used in practical devices involves the use of magnetic ions that exhibit considerably stronger magneto-anisotropies than those that have traditionally been used in the synthesis of large polynuclear clusters, e.g., orbitally degenerate transition metal ions, or heavier elements with Hund's-coupled ($\mathbf{J} = \mathbf{L} + \mathbf{S}$) moments and strong crystal-field interactions. Examples include certain high-symmetry and/or low-coordinate 3*d* transition metal complexes (Fe^{I} [19], Fe^{II} [93, 94], Co^{II} [95–97], even Ni^{II} [98]), as well as elements further down the periodic table such as the 4*d*, 5*d*, 4*f,* and 5*f* elements [99–102]. The discovery in 2003 of a SMM comprising just a single lanthanide ion sandwiched within a bis-phthalocyanine structure clearly justifies this approach [99], resulting in an explosion of activity focused mononuclear SMMs. More recent efforts have focused on achieving strong exchange within low-nuclearity complexes (dimers, trimers, etc. [103–107]) of highly anisotropic magnetic ions. This has resulted in SMMs with quite dramatic increases in both their anisotropy barriers and the technologically relevant blocking temperature. The current benchmark is an N_2^{3-} radical bridged Tb_2 complex that exhibits hysteresis all the way up to 14 K and a barrier of ~330 K [106], i.e., a factor of 4 to 5 higher than Mn_{12}.

In spite of the relative simplicity of some of the more recent SMMs in comparison to, e.g., Mn_{12}, the strong anisotropy presents a considerable challenge to the HFEPR community because zfs energies often exceed 20 cm^{-1} ($\cong 0.6$ THz). The FDMR [69] and frequency domain fourier transform (FDFT [17, 108]) techniques both represent forms of broadband low-frequency (THz or far-infrared) optical spectroscopy that can provide access to excitations in this range (up to about 1.5 THz). Moderate magnetic fields may also be applied to distinguish magnetic excitations from electronic ones. This approach is becoming more applicable as more labs acquire/develop the appropriate hardware to perform such measurements. Some representative examples where magnetic excitations in the 20−40 cm^{-1} range have been reported include: hexaaqua Fe^{II} [109]; pentacoordinate Ni^{II} [110]; square planar Co^{III} [111]; and low-spin pseudo-octahedral Mn^{III} [112].

An orthogonal approach to the frequency-domain techniques described above involves taking advantage of very high-field magnets. The idea here is to compete the Zeeman interaction against the field-independent terms in Eq. (2), thereby providing access to HFEPR transitions that are highly constrained by the zero-field anisotropy [97, 98, 113]. Two examples of such measurements are given in Fig. 4: the first involves an octahedral $s = {}^3/_2$ Re^{IV} complex with a biaxial magnetic anisotropy [113]. In this situation, a ground state level-crossing ($m_s = -{}^3/_2, -½$) can be induced upon application of a magnetic field parallel to the hard (z-) axis. The location of the level crossing is directly related to the zero-field gap between

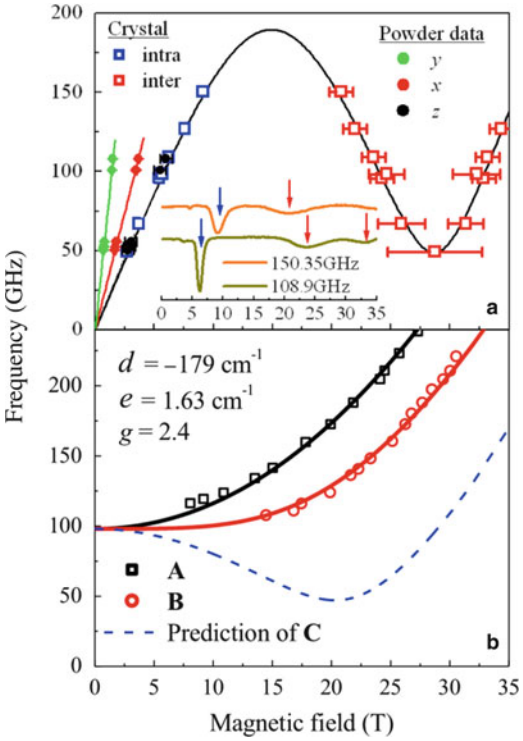

Fig. 4 (**a**) *Main panel*: HFEPR peak positions for a single-crystal of $(NBu_4)_2[ReCl_4(CN)_2]$ at 1.3 K (*open squares*), with the field aligned close to the *z*-axis of the $\overleftrightarrow{d}$ tensor. Intra-Kramers powder peak positions are also included in the low-field region (*solid circles*). The *solid lines* are the best simulations of the peak positions employing Eq. (2). *Inset*: representative high-field spectra obtained at the two indicated frequencies. Reprinted with permission from [113]. Copyright 2012 American Chemical Society. (**b**) HFEPR peak positions for a single crystal of [Ni(Me_6tren)Cl](ClO_4), with the field aligned within the hard plane. A Jahn-Teller distortion gives rise to three molecular orientations, *A*, *B*, and *C*, resulting in multiple resonance branches (see [98] for details). The *solid lines* represent the best fit to Eq. (2) for peaks *A* and *B*, with the obtained zfs parameters given in the figure; the *dashed line* represents the predicted locations of transitions associated with the *C* orientation. Reprinted with permission from [98]. Copyright 2013 American Chemical Society

the two Kramers doublets. Importantly, EPR transitions can be detected at relatively low frequencies (50–100 GHz), in the vicinity of the level-crossing, enabling the use of highly sensitive cavity perturbation methods [16, 114]. Cw HFEPR facilities exist at the US National High Magnetic Field Laboratory (NHMFL) in Florida [115], providing magnetic fields up to 45 T, while experiments at the Dresden High Magnetic Field Laboratory in Germany can be performed in pulsed magnetic fields of up to 70 T [14, 116]. A rough rule of thumb gives 28 GHz/T (~1 cm^{-1}/T for $g = 2$) of tuning, i.e., ~1.3 THz (or 45 cm^{-1}) in Florida and ~2 THz

(or 70 cm^{-1}) in Dresden. These ranges can be extended by combining high-fields and high frequencies (up to 1 THz at both facilities); under the right conditions, the two can add so that zfs energies of order 80–100 cm^{-1} become directly accessible [98]. One may obtain exceptionally tight constraints on all of the relevant parameters of the spin Hamiltonian by conducting measurements over a wide range of frequencies, then performing fits to so-called "Florida Maps" (see, e.g., Fig. 4).

Figure 4b displays a second example involving an orbitally degenerate trigonal-bipyramidal Ni^{II} (d^8) complex with easy-axis anisotropy [98]. The zero-field spectrum consists of a pair of low-lying singlets that are very well isolated from the next singlet on account of an unusually high axial anisotropy associated with this coordination geometry. The low-lying singlets are split by a rhombic e term, which can be directly measured from the zero-field intercept ($=2e$) in Fig. 4b. However, the third singlet is estimated to lie >3 THz above the low-lying singlets, rendering it inaccessible to essentially any currently available EPR spectrometer. A solution to this problem involves application of a magnetic field transverse to the easy-axis, with the goal of reaching a regime where the transition energy/frequency between the low-lying singlet levels depends linearly on the applied field. Extrapolation of the linear region back to zero-field provides a direct measure of the axial anisotropy, in this case the axial d parameter if one chooses to approximate the ion as a spin-only $s = 1$ species. The linear regime has not yet been reached, even at the highest field in Fig. 4b. However, fits to the data suggest a huge d value in the range from -120 to -180 cm^{-1}, which may be a record determination on the basis of EPR [98].

We conclude this section with an example involving a Ho^{III} ($4f^{10}$) SMM encapsulated within a high symmetry polyoxometallate (POM) cage [102]. The encapsulation preserves the intrinsic properties of the nanomagnet outside of a crystal. Consequently, these compounds are of potential interest in terms of the types of molecular spintronics applications discussed in the following section [8, 9]. A significant magnetic anisotropy arises due to a splitting of the Hund's coupled total angular momentum ($\mathbf{J} = \mathbf{L} + \mathbf{S} = 8$) ground state in the POM ligand field. The high symmetry again gives rise to a pair of isolated low-energy singlets, akin to the preceding Ni^{II} example. EPR studies at 50.4 GHz (Fig. 5) reveal a highly anisotropic eight line spectrum corresponding to transitions between the low-lying Zeeman-split $m_J = \pm 4$ components of the $J = 8$ multiplet, split by a strong hyperfine interaction with the $I = 7/2$ Ho nucleus (100% natural abundance) [102]. Meanwhile, X-band (9 GHz) studies reveal the presence of an appreciable zero-field tunneling gap of ~9 GHz between the $m_J = \pm 4$ states, leading to a highly non-linear field-dependence of the spectrum at low-energies (see Fig. 5 [102]). The tunneling gap provides important information concerning the transverse components of the ligand-field that are inaccessible by other experimental methods. It has been postulated that the tunneling gap could provide an optimal operating point for coherent spin manipulations at X-band, which leads naturally into the next section dealing with pulsed EPR applications.

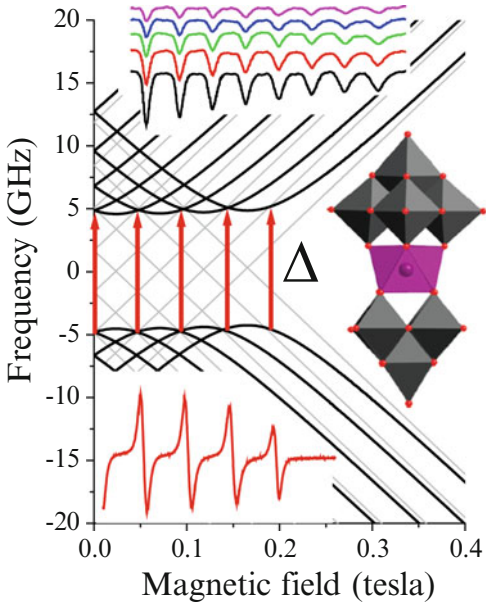

Fig. 5 Multi-frequency, single-crystal EPR spectra for a $Na_9[Ho_{0.25}Y_{0.75}(W_5O_{18})_2]$ complex (*right inset*), with the field applied parallel to the *z*-axis of the zfs tensor. Measurements at 50.4 GHz (*top*) reveal an eight-line spectrum corresponding to transitions within the lowest $m_J = \pm 4$ crystal field levels of the Hund's coupled $J = 8$ ground state, split by a strong hyperfine interaction with the $I = 7/2$ Ho^{III} nucleus. 9.7 GHz measurements (*lower-left*) reveal the presence of an appreciable tunneling gap, $\Delta \approx 9$ GHz, between the $m_J = \pm 4$ states, leading to a highly non-linear field-dependence of the Zeeman levels at low-frequencies (main panel – *dark curves*). The 50.4 GHz data constrain the *z*-components of the Landé and hyperfine tensors, while the 9.7 GHz data indicate the existence of a significant off-diagonal $B_4^4 \hat{O}_4^4$ crystal-field interaction (*faint lines* denote the Zeeman levels in the absence of this interaction). Reprinted with permission from [102]. Copyright 2012 Royal Society of Chemistry

2.3 Pulsed EPR

We conclude this section on EPR by briefly reviewing the growing number of recent pulsed EPR studies involving MNs. These methods are employed primarily to obtain dynamical information related to molecular spin dynamics, as opposed to the static spectroscopic details described in the preceding sections. Nevertheless, one can often infer important information concerning the static spin Hamiltonian based on, e.g., a theoretical understanding of the magnetic field or temperature dependence of relaxation times. More importantly, knowledge of these relaxation times/mechanisms is of crucial importance if one is to eventually employ MNs in spintronics applications. Experiments involve the use of coherent pulses of microwave radiation that are tailored to produce controlled rotations of the magnetization within a sample. The basic principles of pulsed EPR [117] are similar to pulsed NMR. The main challenge concerns the much faster electronic relaxation rates in

paramagnetic solids, requiring large microwave powers in order to achieve coherent operations on sufficiently short timescales. For this reason, applications of pulsed EPR have significantly lagged those of NMR. Nevertheless, recent advances in microwave technologies have translated into significant increases in the performance of pulsed EPR spectrometers. For the most part, commercial systems operating at relatively low frequencies (9/34 GHz) have led the way. Sophisticated spectrometers operating at higher frequencies (>90 GHz) are now becoming available – both home-built [118–120] and from commercial vendors.

Most of the employed pulsed EPR methods rely on the Hahn-echo sequence in which a $\pi/2$ pulse first rotates the magnetization into the *xy*-plane. This magnetization is then allowed to evolve for a time τ, after which it is refocused by means of the π pulse, resulting in an echo at a time 2τ after the initial tipping pulse. Refocusing only occurs if the spins retain phase coherence during the 2τ evolution time. Indeed, by measuring the echo amplitude as a function of the delay time τ, one can directly measure the phase memory time T_2. Variations on the Hahn-echo sequence enable measurements of many other quantities such as the longitudinal relaxation time, T_1, and dipolar couplings to nearby nuclei and other electron spins [117]. Because of the need to retain phase coherence during the Hahn-echo portion of the sequence, one usually has to go to considerable lengths to ensure that the T_2 times in the sample of interest are as long as possible. Thus, experiments are typically performed at low temperatures. However, strong decoherence may remain even at liquid helium temperatures, due to fluctuating dipolar fields generated via energy conserving electron and nuclear spin-spin cross relaxation (so-called flip-flop) processes [121]. Consequently, many other measures are often taken to improve the outcomes of such measurements such as dilution of the paramagnetic species and deuteration of solvents.

The use of pulsed EPR in the study of paramagnetic molecules (including many polynuclear transition metal complexes) goes back well over 25 years [122–124], predating even the discovery of SMMs [1]. These earlier investigations focused on obtaining structural information from biochemically important molecules, e.g., the Mn_4 cluster within the photosynthetic reaction center of Photosystem II [123]. Because of the need for long coherence times, many of the tricks employed in more recent EPR studies have been known to the biochemistry community for a long time, e.g., the use of deuterated solvents to reduce the amplitude of nuclear dipolar field fluctuations [125–127]. The first pulsed EPR study that focused specifically on the possible application of MNs in quantum information processing (QIP) targeted frozen solutions of antiferromagnetically coupled Cr_7M rings (<0.2 mg/ml in Toluene, with M = Ni and Mn) [128, 129]. Measurements were performed in a commercial X-band (9 GHz) spectrometer, and a phase memory time of $T_2 \approx 3$ μs was deduced in deuterated samples of the spin $S = ½$ Cr_7Ni compound at low temperatures [128], comparable to results found in biochemical studies [123, 127]. On the basis of these measurements, it was concluded that the deployment of MNs in QIP applications would be feasible, opening the door to many similar investigations. Subsequent chemical modifications of the molecular structure of the Cr_7Ni compound, aimed at minimizing environmental decoherence

sources, have demonstrated phase memory times of up to 15 μs [130]. Meanwhile, the possibility of propagating quantum information between Cr_7Ni molecules via aromatic linkers has also been explored in-depth [131].

The next milestone involved the observation of Rabi oscillations – quantum oscillations resulting from the coherent absorption and emission of photons. The first such study concerned a trinuclear oxo-centered Fe^{III} ($s = {}^5/_2$) complex that possesses a well-isolated collective $S = ½$ ground state [132]. The complex was again diluted into a frozen acetone solution in order to achieve long phase memory times (2.6 μs at 5 K). Although Rabi oscillations were observed, they decayed rather rapidly (in less than 120 ns). Shortly thereafter, results were reported for a much larger antiferromagnetic V_{15}^{IV} MN embedded within a non-magnetic host (a surfactant that envelops the V_{15} cluster, thereby ensuring that molecules do not interact strongly with each other) [133, 134]. This work was motivated by a much earlier theoretical proposal suggesting that the highly symmetric V_{15} molecule could be a suitable prototype for QIP [6]. In spite of its large size and complexity, the low energy spectrum is relatively simple, consisting of two doublets ($S = ½$) and a quartet ($S = {}^3/_2$), well isolated from a quasi-continuum of states some 250 K above. The main goal of this work was to observe Rabi oscillations associated with the collective $S = ½$ ground spin states, since these are the ones that would be employed for QIP. In fact, in the original studies, performed at a relatively high temperature of ~4 K, Rabi oscillations corresponding to both the $S = {}^3/_2$ and $S = ½$ states were observed; the Rabi oscillation frequencies, Ω_R, differ considerably for the two cases, so they can be selectively excited. However, the authors were subsequently unable to confirm that the $S = ½$ signal was intrinsic to the V_{15} molecule after suggestions that it might be due to a paramagnetic background signal associated with the X-band cavity [135, 136]. More recent studies, performed at a lower temperature of 2.4 K, have definitively shown evidence for the $S = ½$ oscillations, thereby demonstrating the possibility of QIP in the ground states of V_{15} [137].

The early pulsed investigations focused mainly on antiferromagnetic molecules with spin-½ ground states, in part because this is the simplest possible quantum system that can easily be studied using commercial pulsed X-band EPR spectrometers, but also because the small magnetic moment provides maximal protection against environmental decoherence. However, it had previously been proposed that one could implement Grover's search algorithm using the eigenstates of high-spin SMMs such as Mn_{12} and Fe_8 [7]. The first major challenge in cases involving SMMs is the strong magnetic anisotropy, which dramatically broadens the EPR spectrum. Thus, a pulsed measurement performed (in field) on a frozen solution of randomly oriented SMMs would address only a tiny fraction of the molecules in the sample (due to the finite bandwidth of the pulses). Moreover, a high frequency pulsed EPR spectrometer is a prerequisite for studies of most SMMs, for which the technology lags significantly behind that of X-band instruments. A clever solution to these problems involved selecting a SMM for which the EPR excitation frequency from the ground state (the zfs) matched that of a commercial W-band

(94 GHz) instrument in zero applied magnetic field. The chosen compound was $[Fe_4^{III}(acac)_6(Br\text{-}mp)_2]$ (Fe_4 [138]), which possesses a spin $S = 5$ ground state and easy-axis anisotropy. Experiments were again performed on dilute solutions to mitigate molecular spin-spin decoherence, yielding a maximum phase memory time of 630 ns at 4.3 K. Rabi oscillations were also clearly observed. Because the measurements were performed without an external magnetic field, the orientational disorder did not affect the distribution (spread) of excitation frequencies. Thus, a large fraction of the molecules lie within the excitation bandwidth of the employed pulses. However, the orientational disorder does influence the Rabi frequencies, likely explaining the short-lived Rabi oscillations.

An obvious solution to the problem of orientational disorder would be to study single crystals. However, one then runs into the problem of strong electron spin-spin decoherence due to the high concentration of molecules. An ingenious trick that more-or-less completely suppresses this decoherence involves performing EPR measurements at high frequencies and low temperatures [121]. The high frequency (f) ensures that the ground state is well separated from the first excited state. If the temperature (T) is then reduced so that $k_BT \ll hf$, the molecular spin system will maintain near 100% spin polarization. Electronic spin flip-flop processes are completely suppressed in these circumstances (because all spins are aligned). In other words, even though the host crystal is highly magnetized, it is essentially non-magnetic insofar as its magnetization is completely static. The commercial W-band spectrometer employed in the preceding investigation does not meet the $k_BT \ll hf$ condition, because 94 GHz is equivalent to ~4.5 K and the base temperature of the system is not much below this. For this reason, such studies have only been possible up to now using home-built pulsed EPR spectrometers [118], with almost all of the work performed at the NHMFL. The landmark study involved the Fe_8 SMM, for which spin-echo measurements of T_1 and T_2 were performed on an oriented crystal at 240 GHz ($\cong 11.5$ K) and 1.27 ± 0.05 K, in a magnetic field of 4.566 T [139, 140]. A phase memory time of ~700 ns was obtained under these conditions. Although this high-field approach may not be as attractive for potential applications in comparison to the zero-field method described previously [138], it has enabled very detailed investigations of the underlying decoherence mechanisms in SMM crystals [140, 141].

One can take the single-crystal approach further by diluting magnetic molecules into an isostructural non-magnetic host crystal, thus ensuring good alignment of the magnetic species. This approach is challenging for polynuclear systems because the magnetic and non-magnetic elements tend to scramble during the formation of the crystal, leading to a mixture of various mixed-metal species [83]. However, there are a few examples where this can work without scrambling [142]. In one very recent example, spin-echo measurements were possible for Cr_7Zn ($S = {}^3/_2$ ground state) doped into the isostructural Ga_7Zn host (0.3% Cr_7Zn by mass) [143]. Phase memory times approaching 1 μs were found in this example, with good prospects for increasing this value upon further dilution. Rabi oscillations were also detected. By contrast, magnetic dilution of mononuclear species into non-magnetic host

crystals is typically more straightforward, particularly in the case of lanthanides [102]. Indeed, this approach has been widely employed for pulsed EPR studies of magnetic ions embedded into more traditional (non-molecular) solids (see, e.g., [144]). A few studies involving mononuclear lanthanide molecular magnets have recently been reported, particularly involving the isotropic Gd^{III} ion [145, 146]. The prospects for future advances involving related materials look particularly promising [8, 9].

3 Magneto-Optical Techniques

Applications of SMMs in fields such as spintronics and quantum computing will require, as a first step, the deposition of isolated molecules onto surfaces while retaining SMM behavior, so that individual molecules can be manipulated and their behavior specifically employed. In this sense, evolution of characterization tools is required to be able to determine magnetic properties at the nanoscale and, moreover, with surface sensitivity.

Magneto-optical and X-ray based techniques turn out to be very suitable for the spectroscopic characterization of MNs since they allow for high sensitivity and high spatial resolution. One can find different techniques according to the configuration and type of radiation used, either uv/visible or X-ray. In all cases, the magnetic signal is obtained from the dependence on the initial and final states of the transition associated with the absorbed wavelengths, being thus chemically selective in some cases, and also allowing for magnetic measurements as a function of an applied external field, e.g., magnetization hysteresis cycles.

3.1 Magnetic Circular Dichroism and Magneto-Optical Kerr Effect

MCD takes advantage of the differential absorption (dichroism) of left and right circularly polarized light by a sample under the presence of a magnetic field parallel to the propagation direction. It is typically applied in the visible to ultraviolet spectral range and, thus, requires molecular samples to be either transparent or in a solution state that allows for light transmission. By contrast, the magneto optical Kerr effect (MOKE) measures the rotation of the polarization angle after reflection of the electromagnetic wave from a magnetic sample under the presence of a magnetic field, allowing for the characterization of magnetic moments of molecular materials deposited onto opaque substrates, achieving sensitivities of up to 10^{-12} emu. The development of nanoMOKE technology has increased the spatial resolution, leading to surface mapping capabilities of magnetic properties with a resolution close to the intrinsic diffraction limit dictated by the employed

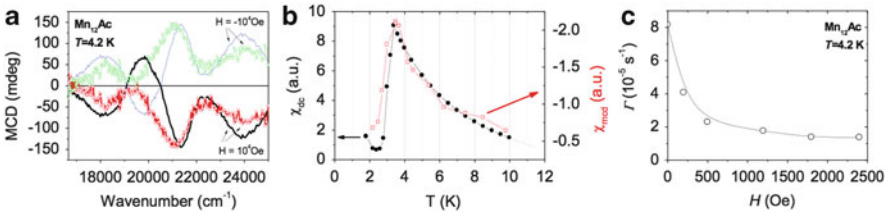

Fig. 6 (**a**) MCD spectra of $Mn_{12}Ac$ in a 1:1 frozen solution of CH_2Cl_2:toluene (*solid curves without symbols*) and 1:2 CH_3CN:dmf (*solid curves with open circles*), at applied magnetic fields of 10^4 Oe and -10^4 Oe (*labeled in the figure*). (**b**) Zero-field-cooled magnetization measurements of $Mn_{12}Ac$ in a 1:1 glass of CH_2Cl_2:toluene, in an applied field of 10^3 Oe; *solid circles* indicate SQUID measurements (referred to the *left axis*) and the *open squares* are the MCD measurements (referred to the *right axis*). (**c**) Magnetization relaxation rates determined from MCD measurements at $T = 4.2$ K, as a function of the applied magnetic field. The increase of the MCD signal decay rate at low fields is indicative of acceleration of the relaxation due to resonant quantum tunneling. Adapted with permission from [151]. Copyright 2004 American Physical Society

wavelength. Moreover, the degree of rotation of the polarization is sensitive to the orientation of the magnetic moment with respect to the surface, allowing for a determination of the orientation of the magnetic anisotropy of thin films of SMMs. Since this technique offers high temporal resolution, it is also highly suitable for studies of magnetization dynamics on surfaces. Some examples include the determination of magneto-optical constants of paramagnetic thin films of phthalocyanine (Pc) molecules such as CuPc by MOKE [147, 148], as well as the interaction of related molecules with a ferromagnetic substrate [149]. However, the use of MOKE for SMM characterizations has not been extended, mainly due to the requirement for low temperature measurements.

Coming back to measurements in absorption, the intensity of the MCD signal depends on the ground and excited state parameters, determined by the *g* factor and zfs, and is thus associated with the degree of spin-orbit coupling, varying with temperature and magnetic field strength. This technique, used initially to perform magnetic characterization of Mn_{12} derivatives isolated in different organic glasses, or embedded in polymeric films [150, 151], has been shown to be a powerful tool for revealing SMM behavior [151–153], and for determining zfs parameters [154]. It is thus complementary to EPR. The study of the thermal and field dependence of MCD signals at very low temperatures also led to the first observation of magnetic hysteresis cycles and relaxation rates of completely isolated SMMs, as shown in Fig. 6, demonstrating that the magnetic anisotropy, the SMM behavior, and also the QTM relaxation are not intrinsically lost when the molecules are isolated in an organic glass [150–152].

Nowadays, MCD is commonly used for the low temperature characterization of magnetic hysteresis cycles of many different types of SMM, generally in frozen solutions or transparent thin films. Several derivatives of Mn_{12} have been studied by MCD in different environments such as an amorphous matrix, Langmuir Blodgett films, directly grafted onto Au surfaces [155], and sprayed onto transparent LiF

substrates [156]. More recently, one can find other examples of molecular magnets studied by MCD: Fe_4 molecular clusters diluted in different polymeric matrices [157], weakly exchange coupled transition metal dimers [158], Ni_4 cubane molecular magnets in a dilute solution [154], mononuclear Dy^{III} SMMs in solution [159], as well as different examples of bis(phthalocyaninato)lanthanide SMM complexes [153, 160] and double decker systems [161]. In this latter case [160], it has been proven that the MCD technique can be used to determine the magnetic properties of different redox states of the same complex, without interference of the preparation of the solid state solution on the results. Moreover, MCD spectroscopy can be used to determine not only the single-ion anisotropy, but also the molecular zfs, which is crucial for understanding the origin of magnetic anisotropy in SMMs [149, 153, 154, 158, 160, 162–165].

Even though it is found that some of the MNs studied by MCD do not retain their SMM properties when deposited on surfaces [155], it is not thought that the absorbance of light resulting from the MCD measurement is responsible for perturbing the natural SMM behavior. Instead, major distortions have mainly been ascribed to critical molecule-surface interactions, or matrix-induced strains [157]. However, absorption of radiation at optical wavelengths can drive changes in the magnetization at low temperatures by triggering phonon-assisted spin-transitions that lead to fast relaxation rates [166]. This can result in the loss of hysteresis properties of SMMs at certain temperatures when measured by SQUID magnetometry under light irradiation (or even by XMCD – see below) that can be wrongly attributed to damage generated by the beam (since the electrons involved in the light absorption process lie at the very heart of the SMM behavior), or to an intrinsic loss of magnetic anisotropy due to the molecular environment [167].

3.2 X-Ray Magnetic Circular Dichroism

XMCD is a synchrotron spectroscopic technique based on the principle that resonant circularly polarized photons are differently absorbed by a magnetic material depending on their helicity relative to the sample magnetization. In XMCD, the photon propagation direction is aligned parallel to the magnetic field and, thus, the quantization (z) axis. In this case, following perturbation theory, the absorption cross-sections for left (L) and right (R) circularly polarized photons can be expressed as:

$$\sigma_{L,R}(\omega) = 4\pi^2 \alpha \hbar\omega \sum_{\phi,l} (l/d_l) \left| \langle \phi | \boldsymbol{\varepsilon}_{L,R} \cdot \mathbf{r} | l \rangle \right|^2 \delta\left(E_\phi - E_l - \hbar\omega\right). \tag{5}$$

Here, $\hbar\omega$ is the energy of the incoming X-rays, α is the fine structure constant, $|l\rangle$ and $|\phi\rangle$ are the initial and final state wave functions of the system, and the delta distribution insures energy conservation. The degeneracy of the ground state is d_l,

and $\boldsymbol{\varepsilon}_{L,R}$ are the polarization vectors [$\boldsymbol{\varepsilon}_L = \sqrt{2}(1/2, \mathrm{i}/2, 0)$ and $\boldsymbol{\varepsilon}_R = \sqrt{2}(1/2, -\mathrm{i}/2, 0) = (\boldsymbol{\varepsilon}_L)^*$] corresponding to the left and right circularly polarized photons propagating along z. The dichroic signal is the difference, $\sigma_L(\omega) - \sigma_R(\omega)$, and it is non-zero when time-reversal symmetry is broken by a net magnetic moment of the system, either due to spontaneous or field-induced magnetic order.

One of the advantages of this technique is its very high surface sensitivity since it has been used to study the magnetism of sub-monolayers of magnetic atoms and molecules on surfaces using the total electron yield (TEY) detection mode [168]. Even more important is its chemical sensitivity, which allows one to specifically probe the magnetic behavior of a given element in a molecule and, moreover, to determine element selective spin and orbital moments separately in heteronuclear systems. Another very appealing aspect that is very useful when studying fragile SMMs on surfaces is the fact that XMCD is a spectroscopic method and, thus, allows for verification of the integrity of the molecules under study by measuring their electronic structure, oxidation, and their magnetic properties [169].

The first examples of SMM characterization with XMCD are quite recent, focusing on Mn_{12} molecules adsorbed on gold surfaces [167, 170], for which a redox instability of the Mn_{12} complexes was observed due to partial reduction of Mn^{III} to Mn^{II}, accompanied by structural rearrangements. These initial studies launched a debate about the suitability of XMCD for SMM studies, since the excitation of core electrons of the molecule could be equivalent to demagnetization effects. However, the following explosion of experiments using XMCD to study a range of SMMs on surfaces, using various different deposition methods [171], provides clear evidence that the technique is *not* incompatible with such SMM characterizations. Examples include: Fe_4 (Fig. 7 and [172–177]) and the isostructural heterometallic Fe_3Cr complex [177, 178] deposited and grafted onto Au surfaces using different covalent groups; Cr_7Ni antiferromagnetic rings [179–182]; the endohedral SMM DyScN@C80 [183]; and double-decker Tb^{III} complexes with phthalocyanine ligands [184–188]. In fact, it seems that Mn_{12} is one of the more fragile examples when deposited on surfaces, showing a strong tendency for reduction of Mn^{III} to Mn^{II}, even in the presence of a buffer monolayer of acid that decouples the molecule from the substrate and minimizes induced perturbations [189]. It seems, therefore, that Mn_{12} is particularly unstable, and that it cannot survive many of the widely employed deposition processes such as sublimation. However, a very recent example of the observation of Mn_{12} on a Bi (111) surface deposited directly by gentle tip deposition using a scanning tunneling microscope (STM), as well as recent measurements of its quantum behavior when deposited on metallic and thin-insulating surfaces by optimized electrospray ion beam deposition [190], opens up new expectations for the assessment of magnetic properties of SMMs on solid surfaces [191]. Meanwhile, submonolayers of Mn_6 SMM derivatives deposited onto Au surfaces [192, 193] show a decrease of the average Mn^{III} spin moment when compared to relatively thick films [194]. However, in this case, the Mn^{III} oxidation state (and, hence, the local moment) is preserved, and the reduced average moment is attributed to local distortions of the Mn environment that modify the Mn-Mn exchange coupling.

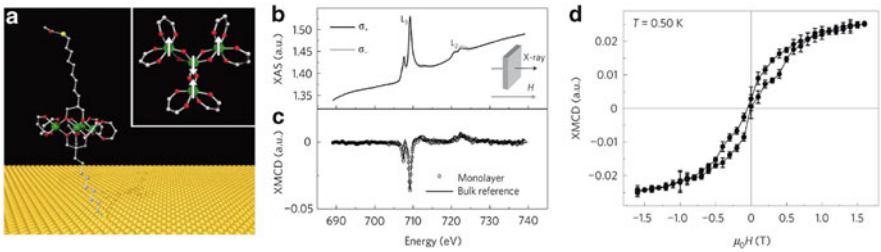

Fig. 7 (**a**) Schematic representation of a Fe_4 derivative bearing a thiolate-terminated aliphatic long chain attached to a gold surface; the *inset* depicts the magnetic core of the Fe_4 molecule with *arrows* indicating the ground-state spin arrangement. (**b**) The iron $L_{2,3}$-edge X-ray absorption spectra (*XAS*) using left-(σ_+) and right-(σ_-) circularly polarized photons, in a magnetic field of 3 T, recorded for a monolayer of the Fe_4 molecules at a temperature of 0.50 K. (**c**) XMCD spectra for a Fe_4 monolayer and a bulk sample. (**d**) A magnetic hysteresis loop obtained for the Fe_4 monolayer, monitored through the XMCD intensity, at a field sweep rate of 2 mTs^{-1}. Adapted with permission from [172]. Copyright 2009 Nature Publishing Group

In contrast to the Mn examples, the Fe_4 SMM seems to easily survive different deposition processes, and monolayers of Fe_4 on Au surfaces preserve their butterfly-shaped hysteresis cycles down to 0.5 K [172, 174, 175], either when adsorbed onto the surface or even when covalently grafted using appropriate ligands [176]. Examples of XMCD hysteresis cycles for Fe_4 derivatives covalently bonded onto Au surfaces are shown in Fig. 7d and in [195]. These results, together with the previously cited ones, demonstrate that there are no fundamental limitations that preclude the observation of magnetic hysteresis when SMMs are wired to a conducting substrate. Moreover, similar to the MCD results obtained for dilute frozen solutions, XMCD has been employed in order to demonstrate that SMMs preserve their quantum properties on surfaces: monolayers of oriented $Fe_4(L)_2(dpm)$ [where H_3L is 7-(acetylthio)-2,2-bis(hydroxymethyl)heptan-1-ol and HDPM is dipivaloylmethane] SMMs grafted onto Au with short aliphatic chains show evidence for resonant QTM by means of the characteristic steps in their hysteresis cycles (see [195, 196]). These investigations went as far as demonstrating that the QTM resonance fields (hysteresis loop steps) displayed the expected dependence on the orientation of the applied magnetic field relative to the normal to the surface, confirming the ordering of the magnetic easy-axis direction with respect to the Au surface. Finally, the element selective capabilities of XMCD allow for the determination of the relative alignment of the magnetic moments of different ions. As an example, it has been shown that the ferrimagnetic interaction between Fe and Cr moments in the Fe_3Cr complex is also preserved when deposited onto a surface [177, 178].

The advantage of element selectivity is a key factor in the study of the origin of magnetic anisotropy in MNs. Cr_7Ni antiferromagnetic rings deposited on surfaces are a paragon for the study of the interplay between single-ion and overall molecular anisotropy in complex polynuclear systems. Submonolayer depositions of Cr_7Ni rings on Au(111) surfaces [179] employing different functionalization

pathways [180], and even self-assembled monolayers deposited by UHV sublimation techniques [181], show very minor perturbations of their electronic structure and magnetic properties, i.e., the oxidation states, local environments, and crystal-field intensities at the Cr and Ni sites remain essentially unchanged. The element selectivity of XMCD also enables confirmation of the antiparallel arrangements of the Cr and Ni magnetic moments. A step forward in XMCD characterization has been achieved by studying the angular-dependence of the dichroic signal, which reveals the magnetic easy-axis direction of the rings with respect to the substrate. Specifically, deep analysis of the angular-dependence of the spectra of ordered monolayers of Cr_7Ni determined that, although the easy-axes of both the Ni and Cr ions are oriented perpendicular to the plane of the ring, the magnetization of the Cr_7Ni molecule is preferentially aligned within the plane of the ring [182]. This can be explained by considering the projection of the easy-axis anisotropy for each ion onto the lowest lying spin states of the molecule, for which the thermally populated $S = {}^3/_2$ multiplet dominates the collective cluster anisotropy at the field/temperature employed for the measurements; the projected anisotropy of this state turns out to be easy-plane. These studies demonstrate that, although XMCD probes the magnetic properties of individual ions, one can still deduce the magnetic anisotropy of an entire molecule via projection methods.

Finally, metal-porphyrins and metal-phthalocyanines are magnetic molecules that have also recently been explored as hybrid systems combining metal and molecular layers for possible use in molecule-based devices. These molecules show excellent chemical stability and, furthermore, they easily organize in perfect 2D networks by spontaneously ordering through lateral hydrogen bonds, thus becoming an archetypal family of metal-organic semiconductors. Initially, XMCD was used to study the interaction between different types of paramagnetic porphyrin molecules and ferromagnetic substrates [197–200]. More recently, XMCD has been applied to the study of slow relaxation of the magnetization of monolayers and sub-monolayers of the double decker $TbPc_2$ SMM deposited onto Cu [184], Au [185], and graphite surfaces [186, 187], together with its neutral and anionic derivatives and, more recently, sublimated onto $La_{0.7}Sr_{0.3}MnO_3$ (LSMO) and Co surfaces [188]. The typical butterfly shaped hysteresis curves are preserved for deposition onto Au and HOPG surfaces, as observed by XMCD at low temperatures, indicating that the intimate interaction with the substrate doesn't destroy the magnetic anisotropy in these cases. A decrease in anisotropy compared to the crystalline phase is observed for sub-monolayer deposition onto Au. Meanwhile, no hysteresis was observed for $TbPc_2$ molecules deposited onto Cu, LSMO, and Co. For Cu, this was attributed to the long times necessary to acquire a typical XMCD magnetization curve. However, it remains unclear as to the origin of the disappearance of the butterfly shaped hysteresis loops in the other cases.

4 Inelastic Neutron Scattering

The neutron, a charge-less particle with a quantum spin of one half, is highly penetrating in matter and an efficient microscopic probe of magnetism. Beams of neutrons for spectroscopy provide unique spatial and temporal information on interaction with magnetic materials. INS measures neutron energy and momentum transfer on interaction with the measured sample, from which the energy of magnetic excitations and aspects of their internal spin structure may be obtained directly. INS probes the magnetism of MNs in the same energy window where exchange interactions and anisotropies exist. The key advantages of a low energy microscopic probe relate to how measurements may be performed in zero or at fixed applied magnetic fields, with excited states being accessed directly along with detailed information relating to their wave functions.

Historically INS has maintained to be a somewhat specialist spectroscopic tool, as investigations of MNs were limited by the requirement of large sample quantities (typically of order 5 g), and the necessity of deuteration of all hydrogen atoms present within investigated samples. Recent advances in INS instrument technology mean that, today, samples on the order of 200 mg are often sufficient, opening up possibilities for the study of single crystal samples and the measurement of polycrystalline compounds with low synthetic yield. Furthermore there is an increasing realization that, in some energy ranges, deuteration is not always imperative as previously thought for the measurement of energy spectra in polycrystalline studies. Altogether, INS is more accessible for the study of MNs than ever before, and the first single crystal investigations have proven to permit the extraction of unprecedented information concerning the internal spin structure of MNs.

In the early days, magnetic dimers were prepared specifically for the investigation of exchange interactions in systems free from the cooperative magnetic effects present within extended magnetic systems. This is where the use of INS first took its foothold in the study of physical phenomena of MNs. These initial works provided a proof of principle, demonstrating how direct access to exchange interactions could be obtained, and how the different types of transitions could be distinguished via the momentum transfer of the INS intensity. Today, the physics of MNs has become a field of research in its own right, and INS plays an integral role in unraveling the properties of increasingly complex MN compounds. There are several reviews available presenting case studies of significant highlights in the application of INS for the study of MNs; see for example [201–204]. The aim of the present review is to outline some examples of seminal INS results, along with a selection of examples that benefited from the most up-to-date advances in instrumentation. Emphasis is made on how instrument development is driving higher levels of spectroscopic detail in magnetic characterization and outlining the new opportunities associated with the investigation of single-crystal MNs.

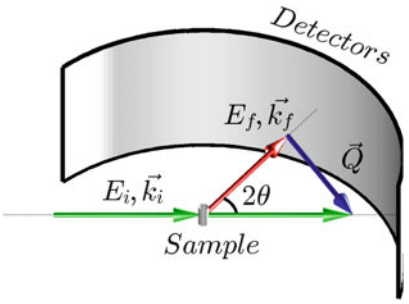

Fig. 8 Inelastic neutron scattering instrument setup; see text for explanation

4.1 General Background to INS

Neutrons provide a useful probe for the study of structure and dynamics in matter from a wide range of scientific disciplines. This is due to the extremely rich interactions that occur between the neutron and the sample under investigation. Neutrons, which have no electrical charge, may have their momenta adjusted to correspond with de Broglie wavelengths comparable to interatomic distances in matter, hence providing a tunable probe of spatial and dynamic correlations. Neutron beams are produced at specialist nuclear reactors or at spallation source facilities. Spallation is a technique where high-energy protons are accelerated into a heavy metal target driving neutrons from the target nuclei. Both spallation and nuclear fission create neutrons of high energy (MeV), and thus a moderator is required to reduce neutron energies appropriate for spectroscopy (typically 0.1–10 meV) [205]. Typically, the magnetic excitations (and zfs in SMMs) match this INS energy window, providing direct access to exchange interactions and anisotropy parameters. The neutron quantum spin angular momentum of $s = ½$ interacts with unpaired electrons of the investigated sample. Consequently when a low-energy neutron is inelastically scattered by unpaired electrons in the measured sample, the change in neutron energy is a large fraction of its initial energy. Measurements of changes in neutron energies upon interaction with the measured sample hence provide a direct probe of magnetic excitations. A typical INS instrument monochromates the incident neutron beam, selecting the initial neutron beam energy (E_i) and momentum ($\hbar \boldsymbol{k_i}$, where $\boldsymbol{k_i}$ is the initial wave vector). Scattered neutrons gain or loose energy on interaction, and arrive at a detector with a final energy (E_f) and momentum ($\hbar \boldsymbol{k_f}$). The energy transfer ($\hbar\omega$) between the measured sample and the interacting neutron beam is expressed in Eq. (6) and the momentum transfer vector ($\boldsymbol{Q}$) is deduced from the scattering angle with respect to the initial and final wave vectors, as expressed in Eq. (7) (see Fig. 8):

$$\hbar\omega = E_i - E_f = \frac{\hbar^2}{2m}\left(\boldsymbol{k}_i^2 - \boldsymbol{k}_f^2\right) \tag{6}$$

$$\hbar\boldsymbol{Q} = \hbar\left(\boldsymbol{k}_i - \boldsymbol{k}_f\right). \tag{7}$$

4.2 Neutron Scattering Cross Section

The cross section (σ) of neutrons with energy in the range from E_f to $E_f + dE_f$, scattering into an individual detector of area $d\Omega$, is expressed in terms of the partial differential cross-section. A general basic expression to describe this, applicable to both nuclear and magnetic scattering, can be derived from Fermi's Golden Rule and is equivalent to the first Born approximation, where the interaction between neutron and sample is considered small enough to be treated as a perturbation [205, 206]:

$$\frac{d^2\sigma}{d\Omega dE_f} = \left(\frac{m_N}{2\pi\hbar^2}\right)^2 \frac{k_f}{k_i} \sum_{nm} p_n \left| \left\langle \boldsymbol{k}_i, n \middle| \hat{O} \middle| \boldsymbol{k}_f, m \right\rangle \right|^2 \delta(E_n - E_m + \hbar\omega). \tag{8}$$

The neutron mass is given by m_N, and E_n and E_m are the eigenvalues for the initial (n) and final (m) states of the scattering system, respectively. The Kronecker delta function (δ) maintains energy conservation within the scattering process. The scattering system has to be in thermal equilibrium, where the occupation of a specified n state is based on the Boltzmann distribution function (p_n). The operator $\hat{O}$ represents the specific interaction between the neutron and the scattering system. Experimentally, large portions of $\boldsymbol{Q}$ and $\hbar\omega$ are measured. Hence it is convenient to express the neutron scattering as a function of these measured dimensions [Eq. (9)]:

$$S(\boldsymbol{Q}, \omega) = \left(\frac{2\pi\hbar^2}{m_N}\right)^2 \frac{k_i}{k_f} \frac{d^2\sigma}{d\Omega dE_f}. \tag{9}$$

Neutron scattering interactions within condensed matter include absorption, nuclear scattering (coherent and incoherent), and magnetic scattering.

4.2.1 Nuclear Scattering

Nuclear scattering is expressed by Eq. (8) with substitution of Eq. (10), the Fermi pseudo-potential for $\hat{O}$.

$$V_{\text{nuc}} = \frac{2\pi\hbar^2}{m_N} b_j \delta(\boldsymbol{r} - \boldsymbol{r}_j). \tag{10}$$

The Fermi pseudo-potential considers the interaction between a neutron (position, $\boldsymbol{r}$) and a nucleus (position, $\boldsymbol{r}_j$), where b_j is the scattering length of the jth nucleus. The scattering length depends on the specific nucleus. When the interacting nucleus (nuclei + neutron) is not near an excited state, the scattering length is real and depends on the neutron spin and the interacting nucleus spin. It is worth noting that, for interacting nuclei near excited states, the scattering length becomes imaginary. In this case, neutron absorption occurs; strong neutron absorbers include

metals such as ^{113}Cd [205] and Gd [207]. Coherent nuclear scattering gives Bragg diffraction peaks and phonons. Incoherent nuclear scattering gives an isotropic elastic contribution and an inelastic response proportional to the vibrational density of states. A large source of incoherent scattering in MNs is from hydrogen which has a particularly large incoherent cross-section. Large quantities of incoherent nuclear scattering can mask the observation of magnetic excitations. In many cases the incoherent nuclear scattering of ligand hydrogen within MNs does not become significant until energies greater than around 2 meV. To alleviate the contribution of incoherent nuclear scattering that sometimes does obscure magnetic scattering, the hydrogen within the investigated MN can be interchanged with deuterium. Deuterium exhibits an incoherent cross-section 40 times less than hydrogen. Distinction between incoherent phonons and magnetic excitation intensities can be made by analysis of the momentum transfer of the inelastic scattering intensity. The intensity of incoherent phonon scattering follows a Q^2 dependence, in contrast to magnetic excitations which exhibit more complex modulations of intensity with respect to Q.

4.2.2 Magnetic Scattering

The magnetic scattering interaction potential [Eq. (11)] resembles the nuclear potential; $F_j(Q)$ is the magnetic form factor, the Fourier transform of the normalized unpaired electron density of the jth atom at position $\boldsymbol{r}_j$ with linear momentum p_j.

$$V_{\text{mag}} = \frac{2\pi\hbar^2}{m_N} p_j F_j(Q)\delta\left(\boldsymbol{r} - \boldsymbol{r}_j\right). \tag{11}$$

The partial differential magnetic scattering cross-section can be determined as in the case of nuclear scattering by substitution of the magnetic interaction potential, Eq. (11), into Eq. (8). For a finite magnetic complex, where unpaired electrons are localized to positions $\boldsymbol{r}_j$, the partial differential magnetic scattering cross section can be written as:

$$\frac{d^2\sigma}{d\Omega dE_f} = \frac{A}{N}\frac{k_f}{k_i}\sum_{n,m} P_n I_{nm}(\boldsymbol{Q})\delta\left(E_i - E_f + \hbar\omega\right), \tag{12}$$

where A = 0.29 *barn* and N is the number of magnetic ions. The INS intensity has an orientation dependence given by the quantity $I_{nm}(\boldsymbol{Q})$, written explicitly in Eq. (13).

$$I_{nm}(\boldsymbol{Q}) = \sum_{jj'} F_j^*(Q) F_{j'}(Q) e^{i\boldsymbol{Q}\cdot(\boldsymbol{r}_j - \boldsymbol{r}_{j'})} \sum_{\alpha\beta} \left(\delta_{\alpha\beta} - \frac{Q_\alpha Q_\beta}{Q^2}\right) \times \langle n|\hat{s}_{j\alpha}|m\rangle\langle m|\hat{s}_{j'\beta}|n\rangle. \tag{13}$$

Equation (13) contains the space and time Fourier transform of the time dependent spin-spin correlations for all permutations of pairs of magnetic moment carrying ions ($\hat{s}_{j\alpha}$ and $\hat{s}_{j'\beta}$) within the MN, where α and β denote the Cartesian coordinates x, y, z. The $(\delta_{\alpha\beta} - Q_\alpha Q_\beta/Q^2)$ factor maintains that the neutron only couples to components of the magnetic moment which are perpendicular to the wave vector $\boldsymbol{Q}$ [205].

The intensity of each given magnetic excitation varies as a function of $\boldsymbol{Q}$ in the first case by the magnetic form factor, $F(Q)$, of the scattering magnetic ions, which results in a decrease in intensity for increasing magnitude of Q. Additionally, the relative positions of the moment carrying ions modulate the scatting intensity within the structure factor $e^{i\boldsymbol{Q}\cdot(\boldsymbol{r}_j - \boldsymbol{r}_{j'})}$ in numeration with the space and time Fourier transform of the time dependent spin–spin correlations, $\left\langle n|\hat{s}_{j\alpha}|m\right\rangle\left\langle m|\hat{s}_{j'\beta}|n\right\rangle$. These correlation terms exhibit all of the information associated with the spin dynamics of the specific excitation.

The correlations are the key quantities describing the detailed spin dynamics of the measured sample. It hence pertains that if large portions of the magnetic scattering contribution to $S^{\alpha\beta}(\boldsymbol{Q},\omega)$ are measured for a MN with a well-defined orientation (i.e., a single crystal), the specific two spin correlations for each magnetic excitation can be extracted directly. To date the majority of measurements concern the investigation of polycrystalline MN samples. In such events $I_{nm}(\boldsymbol{Q})$ is averaged over all spatial orientations of $\boldsymbol{Q}$, a procedure described explicitly in [208, 209]. The orientation averaged scattering function is, hence,

$$S(\boldsymbol{Q},\omega) = \sum_{n,m} P_n I_{nm}(\boldsymbol{Q}) \cdot \delta\big(E_i - E_f + \hbar\omega\big). \tag{14}$$

Selection rules derived from the magnetic scattering cross section, Eq. (12), dictate that neutron scattering transitions should obey the following: $\Delta S = 0, \pm 1$ and $\Delta m_s = 0, \pm 1$. These selection rules allow the energy between different spin multiplets to be probed directly. INS studies of orientation averaged samples still contain important information about the spin dynamics and spatial properties of magnetic excitations via their Q dependence.

4.2.3 Instrumentation

The most convenient means to access large portions of the magnetic scattering function, $S(\boldsymbol{Q},\omega)$, is via the time-of-flight (ToF) technique. Following monochromation, bursts of neutrons with a fixed velocity interact with the sample.

The time elapsed before neutrons arrive at the detectors, set at a fixed distance from the sample, is used to determine the change in neutron velocity and, hence, the energy transfer upon interaction with the measured sample. Similarly, the position of neutron detection resolves the change in neutron momentum on interaction with the sample. Figure 8 shows a schematic of a direct geometry INS instrument. Recently, the development of detector arrays with large position sensitive detectors allows for huge portions of $S(\boldsymbol{Q}, \omega)$ to be accessed, increasing detection sensitivity and special resolution. Conventionally, ToF spectroscopy is performed by selecting a single neutron pulse of monochromatic wavelength from a polychromatic source beam. Contrastingly, the recently developed repetition rate multiplication (RRM) method [210] makes more efficient use of source neutrons, especially at spallation facilities, selecting multiple monochromatic wavelengths at each source pulse, dramatically increasing the repetition rate of ToF. Several of the latest cold neutron spectrometers to come online at spallation source facilities (such as LET at the ISIS facility in the UK [211] and; AMATERAS at MLF, J-PARC in Japan [212]) include RRM, or *multi-*E_i options. These spectrometers enable several dynamical ranges to be measured simultaneously (see Fig. 11 below).

4.3 A Direct Probe of Exchange Interactions

The first investigation of magnetic exchange coupling in a molecule-based magnet by INS was reported by Güdel and Furrer in 1977 [214, 215]. The experiment outlined the measurement of exchange interactions in a dinuclear Cr^{III} complex, $[(NH_3)_5CrOHCr(NH_3)_5]^{5+}$. The complex exhibits antiferromagnetic (AF) coupling between the two Cr^{III} ions. The neutron energy loss showed clear, well defined peaks corresponding to $|S=0\rangle \rightarrow |S=1\rangle$, $|S=1\rangle \rightarrow |S=2\rangle$, and $|S=2\rangle \rightarrow |S=3\rangle$ transitions respectively, see Fig. 9a. The energetic sequence of the transition intensities was established by monitoring the temperature dependence of the observed transitions. At 5 K $|0\rangle \rightarrow |1\rangle$ is observed alone; with increasing temperature, further excited states are revealed. Measuring at different temperatures provides information to distinguish between magnetic and phonon excitations – phonons obeying Bose statistics, whereas electron population of exchange-split levels is governed by Boltzmann statistics. The momentum transfer of the $|0\rangle \rightarrow |1\rangle$ excitation is shown in Fig. 9b. The structure factor for the calculation of the Q dependence of the inelastic transition intensity, for the case of the dimer singlet to triplet excitation, simplifies to give:

$$I(Q) \propto F(Q)^2 \left(1 - \frac{\sin(Q \cdot R)}{Q \cdot R}\right), \tag{15}$$

where R is the distance between the two Cr ions and $F(Q)$ is the magnetic form factor of the Cr ions. Following this proof of principle investigation of 3*d*–3*d*

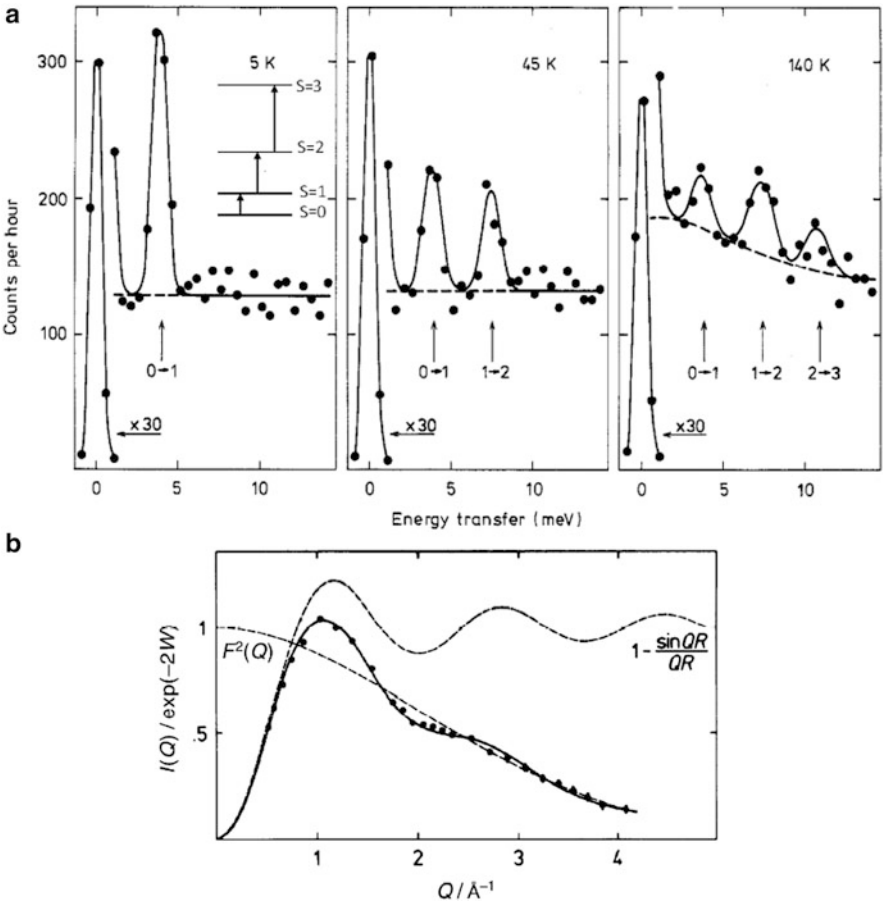

Fig. 9 Magnetic excitations of a polycrystalline sample of the dinuclear Cr^{III} complex, $[(NH_3)_5CrOHCr(NH_3)_5]^{5+}$. (**a**) Energy spectra show how variable temperature measurements access the energy gaps between successive spin states. (**b**) Momentum transfer associated with the transition from $S = 0$ to 1 at 5 K (*black circles*). The *solid* and *dashed curves* are calculations based on Eq. (15). Adapted with permission from [214, 215]. Copyright 1977 American Physical Society and Taylor & Francis

exchange interactions between Cr ions, INS was utilized to investigate the more complex exchange interactions of 4*f*–4*f* and 4*f*–3*d* exchange. Except for Gd^{III}, exchange concerning lanthanide metals (Ln) is complicated by the manifestation of ligand field effects within the same temperature range as the exchange interactions between the magnetic centers. Furthermore, the large spin-orbit coupling of Ln ions means that assumptions about *g* values in applied magnetic fields are not straightforward. For these reasons INS has proven a particularly well suited means for the investigation of Ln exchange. Initial studies concerned Ln^{III} dimers such as $Cs_3Tb_2Br_9$ [216, 217]. The nature and magnitude of Tb-Tb exchange was evaluated within the exchange coupled, lowest energy ligand-field states. Figure 10 shows the

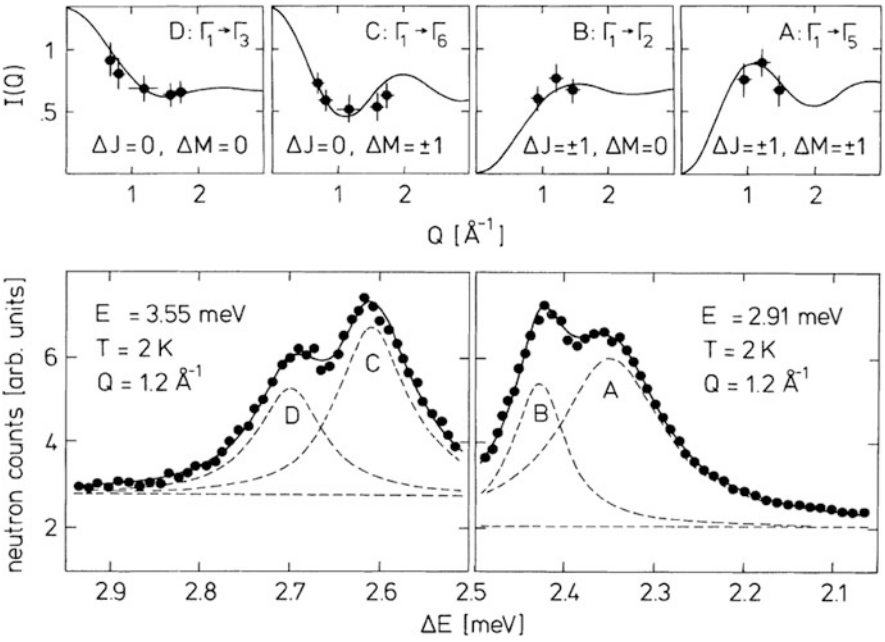

Fig. 10 *Main panel*: neutron energy spectra of a polycrystalline $Cs_3Tb_2Br_9$ dimer compound, resolving transitions to four excited states labeled *A* to *D*. The *top figures* show the different momentum transfers for each of the excitations, which depend on the transition selection rules. Reprinted with permission from [216]. Copyright 1989 American Physical Society

three excitations probed, and their specific Q dependences, measured on the ToF instrument IN5 at Institut Laue Langevin (ILL), Grenoble, France. The four transitions have their own characteristic Q-dependence corresponding to the different wave-functions of the relevant dimer states involved in the observed excitation. This information enabled the deduction of a weak antiferromagnetic Heisenberg exchange interaction of $\mathcal{J} = -0.0049\,\text{meV}$ $\left(\hat{H} = -2\mathcal{J}\boldsymbol{J}_1 \cdot \boldsymbol{J}_2\right)$. This method has proven valuable for detailed investigations of the magnitude, sign, and symmetry of exchange interactions in a wide variety of Ln pairs [218, 219] and mixed dimers of 4*f*–3*d* coupled ions [220].

4.4 Single-Molecule Magnets

4.4.1 Exchange Coupled Lanthanide Based SMMs

A renewed interest has formed in the characterization of Ln based MNs following their utilization for the design of SMMs with large blocking temperatures [99–107, 221, 222]. Since the early investigations of Ln exchange, instrumentation for ToF

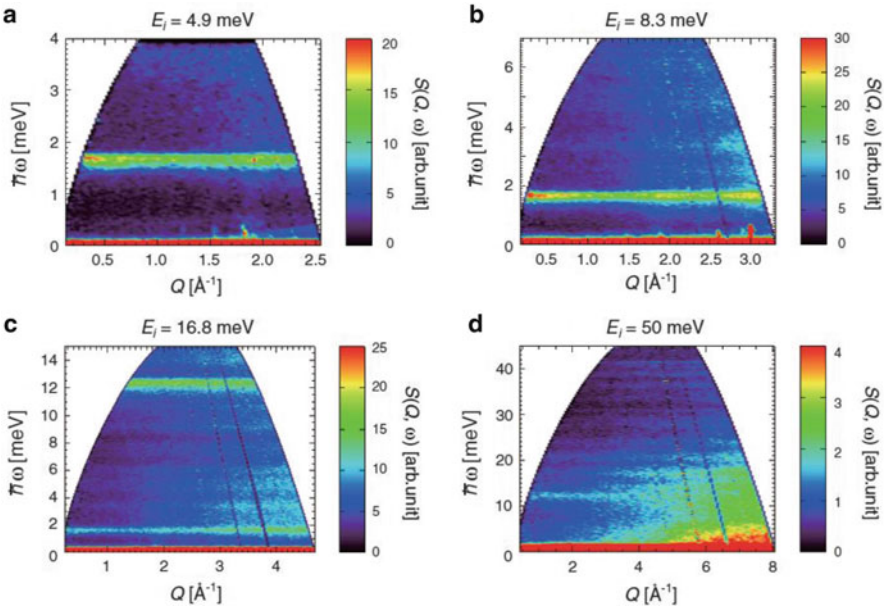

Fig. 11 INS intensity as functions of energy and momentum transfer measured on a Tb-Cu dimer. The respective $S(Q, \omega)$ maps correspond to incident neutron energies of 4.9, 8.3, 16.8, and 50 meV (**a**–**d**, respectively). Measurements were performed simultaneously at 3.5 K using the repetition rate multiplication spectrometer AMATERAS at MLF, J-PARC in Japan. Reprinted with permission from [213]. Copyright 2013 American Physical Society

INS has undergone marked development. The AMATERAS ToF spectrometer was utilized to investigate a Tb-Cu SMM [213] using RRM. In this investigation, four incident neutron energies and wave vectors were selected to probe four $S(Q, \omega)$ dynamic ranges simultaneously. Figure 11 shows the $S(Q, \omega)$ intensity maps measured for the Tb–Cu SMM: two clear magnetic excitation bands are observed at 1.7 and 12.3 meV corresponding to the energy of the Tb–Cu exchange interaction and the transition between the multiplets of the Tb ligand field states. The high instrumental resolution of the AMATERAS spectrometer ($\Delta E/E \sim 1\,\%$) permits resolution of the hyperfine interaction of Cu and Tb, observed as splitting within the 1.7 meV excitation.

4.4.2 Transition Metal SMMs and the Giant Spin Approximation

INS investigations on the first discovered SMMs resolved the zfs without the need for applied magnetic fields, aiding the development of simplified models necessary to understand the manifestation of slow magnetic relaxation and QTM. The first INS investigations were performed on $[Fe_8O_2(OH)_{12}(tacn)_6]^{8+}$ (Fe_8 [223]) and, shortly thereafter, on $[Mn_{12}O_{12}(CD_3COO)_{16}] \cdot 2D_3COOD \cdot 4D_2O$ (deuterated

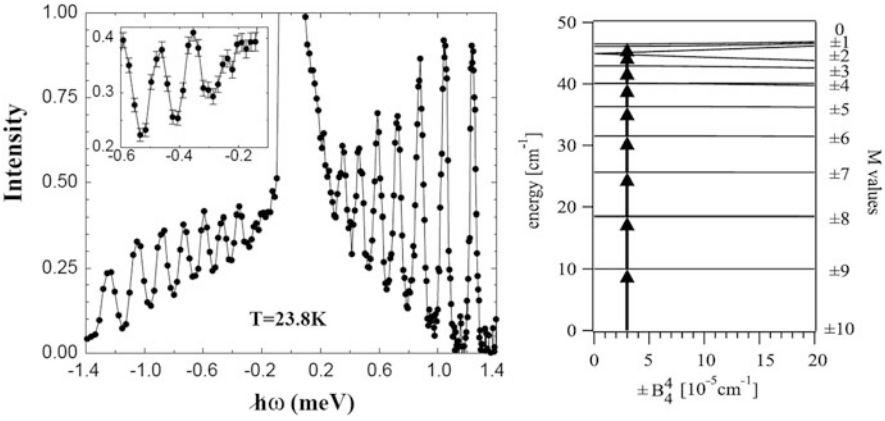

Fig. 12 (*Left*) Neutron scattering intensity as a function of energy transfer for $Mn_{12}Ac$. (*Right*) Zero-field-splitting eigenvalues within the ground state multiplet calculated as a function of the transverse anisotropy term (B_4^4) relevant to QTM. Adapted with permission from [224]. Copyright 1999 American Physical Society

$Mn_{12}Ac$) [224, 225]. In both cases, the advantage of a zero applied magnetic field approach to directly measure zfs within the ground spin multiplet was demonstrated. The observed transition energies and intensities were calculated within the approximation of a single $S = 10$ ground state (the giant spin approximation, or GSA – see Sect. 2.1). Figure 12 shows the neutron scattering energy spectrum for $Mn_{12}Ac$. The measurement determined irregular spacing of transition energies (related to B_4^0), and a reduction in transition intensities at the top of the energy barrier, providing direct spectroscopic access to the transverse Hamiltonian term coefficient (B_4^4) responsible, in part, for the manifestation of QTM. Figure 12b shows how the zero field eigenvalues vary as a function of the B_4^4 coefficient, with arrows labeling the observed INS transition intensities. The B_4^4 coefficient only accounts for QTM for even to even M_S applied field crossings (see Fig. 1), inconsistent with magnetization measurements where QTM is observed at every M_S crossing [29, 30]. Some 5 years later, following an upgrade of the IN5 spectrometer incident neutron flux in 2002 [226], further insight into the quantification of lower symmetry Hamiltonian terms within $Mn_{12}Ac$ could be resolved [43]. In this later investigation, evidence for rhombic anisotropy within a multi-isomer model was quantified, consistent with EPR results [33, 34, 42]. The inclusion of rhombic anisotropy is justified by low temperature X-ray and neutron diffraction analyses [227, 228] which identify hydrogen bonds responsible for transmitting lattice solvent disorder to $Mn_{12}Ac$ clusters, as discussed in detail in Sects. 1.1.1 and 1.1.2. Further INS studies of $Mn_{12}Ac$ went on to investigate pressure induced reduction of axial anisotropy [229] and investigations into the exchange interactions present within $Mn_{12}Ac$ resulting in the identification of several spin excited states [230, 231].

The ability to spectroscopically access exchange interactions and anisotropy based zfs has meant INS is appropriate for studying SMMs where the GSA is no longer appropriate (see also Sect. 2.2). This was the focus of an investigation into the breakdown of the GSA via the characterization of two Mn_6 complexes [232, 233]. The possibility to probe inter-multiplet transitions by INS enabled access to energy levels originating from the excited $S = 11$ manifold. Indeed, the $S = 11$ excited states were identified to be below the anisotropy barrier and nested within the $S = 12$ ground state multiplet. Using a microscopic spin Hamilton, considering exchange between Mn^{III} ions and their individual anisotropy contributions, the properties of the Mn_6 clusters could be described including the demonstration of tunneling pathways involving manifolds of different total spin S.

4.5 *Inelastic Neutron Scattering in Fixed Applied Magnetic Fields*

Elusive physical phenomena such as magnetic frustration induced ground state degeneracy [234–238], and the avoided spin state crossings at critical applied magnetic fields [239], are challenging to quantitatively examine. Understanding the composition of the state wave functions involved is imperative for the rationalization of such phenomena. The application of an applied static magnetic field provides a means to break magnetic frustration induced degeneracy such that the wave functions of the involved spin states can be probed by INS. Likewise, applied fields can be used to access critical points exhibiting interesting quantum tunneling phenomena. It is desirable that electromagnets for ToF INS do not restrict scattered neutron pathways, so as to maximize $S(\boldsymbol{Q}, \omega)$ coverage. The design of such setups in increasingly high magnetic fields, and with broader angular neutron detection ranges, is in continuous development [240] and will provide a marked advance for the study of condensed matter magnetism as a whole.

There have been several successful INS investigations of MNs in applied fields. The IN5 ToF spectrometer was used to investigate the antiferromagnetic molecule $K_6[V_{15}As_6O_{42}]\cdot H_2O$ [241] in applied fields of up to 2.5 T. The employed magnet reduced the vertically accessible detector coverage of the IN5 instrument. However, the portion of $S(\boldsymbol{Q}, \omega)$ obtained proved sufficient to determine the origin of wave function mixing in the frustrated ground state of this system. An isolated spin ½ trimer with equilateral AF exchange is the most fundamental model system to investigate the manifestation of magnetic frustration. If characterized in sufficient detail, the energy levels and wave functions of the system may be solved exactly, in contrast to extended frustrated systems with collective magnetic phenomena [242]. The V_{15} molecule has multi-layered exchange pathways with a V_3 triangle sandwiched between two V_6 rings. Magnetic susceptibility measurements and EPR show that, below 100 K, the two rings above and below a central triangle of V ions lock into a singlet state and, at lower temperatures, the spin dynamics of the system

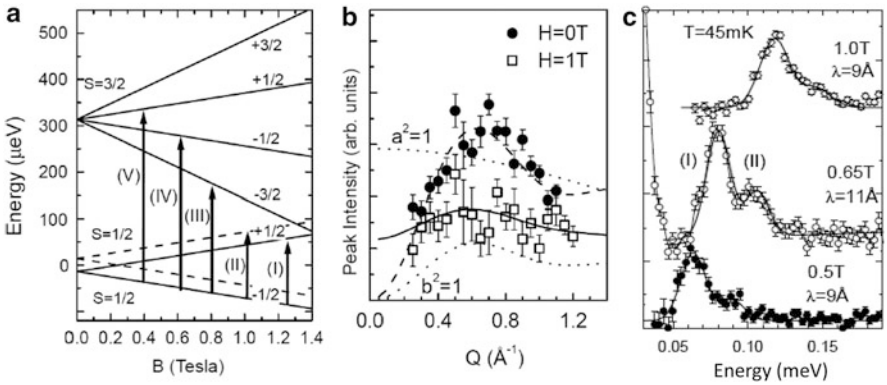

Fig. 13 (**a**) Energy level diagram of V_{15} in applied magnetic field with labels for the observed INS transitions. (**b**) Neutron intensity as a function momentum transfer, Q, for transitions I (at a field of 1 T – *open squares*) and $III + IV + V$ (at 0 T – *black circles* with a simulation denoted by the *dashed curve*); simulations of I were performed according to Eq. (16), both with the inclusion of state mixing (*solid line*) and without (*dotted lines*). (**c**) Use of magnetic field to resolve the low-energy transitions I and II. Adapted with permission from [247]. Copyright 2004 EDP Sciences

are governed by the V_3 triangle which rests on the C_3 symmetry axis of the molecule [243, 244]. A trigonal symmetry triangle of AF coupled spin-½ particles (s_a, s_b and s_c) has a ground state characterized by two degenerate Kramers doublets, $|0, ½, ½, \pm½\rangle$ and $|1, -½, ½, \pm½\rangle$, corresponding to the following basis $|S_{ab}, S_c, S_{\text{total}}, M_S\rangle$. However, low temperature magnetization measurements of V_{15} exhibit butterfly like hysteresis, suggesting a small degeneracy lifting within the ground state, and mixing between the two Kramers doublet states [245]. Initial attempts to account for this non-degeneracy were inconclusive [246]. Only by analysis of INS intensity as a function of Q with applied magnetic field could the internal spin structure of the frustrated triangle be deduced [247]. Figure 13a shows the energy level diagram as a function of applied field, with labels for the accessed INS excitations. With the application of the field, it is possible to resolve the non-degeneracy of the two Kramers doublets (27 μeV). In zero applied magnetic field, the intensity of a $\Delta S_{a,\,b} = 0$ transition is the same as a $\Delta S_{a,\,b} = \pm 1$ transition for an equatorially AF exchange coupled triangle. However, in an applied magnetic field, the intensity of a $\Delta S_{a,\,b} = 0$ transition is three times as intense as a $\Delta S_{a,\,b} = \pm 1$ transition. Figure 13c shows that the intensity of transitions I and II are different in applied field, but not by a factor of three. The Q dependence of transition I is used to quantify the origin of mixing between the $|0, ½, ½, \pm½\rangle$ and $|1, -½, ½, \pm½\rangle$ states. Equation (16) expresses the orientation averaged $I(Q)$ for the specific case of a triangle, where a^2 and b^2 are mixing coefficients for the $S_{a,\,b} = 0$ and 1 states, respectively, R is the interatomic distance, and I_0 is a normalization constant.

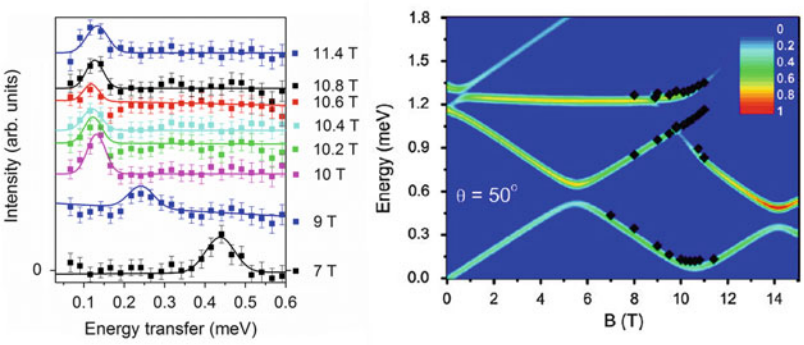

Fig. 14 (*Left*) INS energy spectra for a single crystal of Cr_7Ni, measured at 66 mK and at various fields in the vicinity of an avoided spin state crossing. (*Right*) Measured peak maxima (*black squares*) superimposed on a calculated INS intensity color plot of energy versus applied magnetic field. Adapted with permission from [248]. Copyright 2007 American Physical Society

$$I(Q) = I_0 F(Q)^2 \left[a^2 + \frac{b^2}{3} \left(1 - \frac{\sin(QR)}{QR} \right) \right]. \tag{16}$$

The proportion of mixing found to reproduce the measured Q dependence of I [solid line in Fig. 13b] was found to be represented by the inclusion of a small difference in the exchange coupling between sites s_a/s_b with respect to s_b/s_c and s_a/s_c. Quantification of the energy gap and its origin required neutron scattering. The study ruled out a long-standing theory that Dzyaloshinskii-Moriya (DM) interactions governed the non-degeneracy in V_{15}, showing that the energy gap between the doublets is field independent, in contradiction to a splitting originating from DM exchange.

Mixing between wave functions at avoided spin state crossings has been investigated by INS directly in the heterometallic AF ring $[(C_2D_5)_2NH_2Cr_7NiF_8(O_2CC(CD_3)_3)_{16}]$ (Cr_7Ni [248]). The inclusion of a Ni^{II} ion within an AF ring of 8 Cr^{III} ions breaks the ideal ring symmetry. The ToF Disk Chopper Spectrometer at the NIST Center for Neutron Research was used to probe a single crystal of Cr_7Ni in magnetic fields up to 11.4 T. The avoided crossing between the $S = ½$ ground state and the $S = {}^3/_2$ first excited state corresponds to a coherent oscillation in the total spin between $S = ½$ and ${}^3/_2$. To confirm this scenario experimentally the spin dynamics of the avoided crossing gap have to be directly probed in the frequency domain. INS is a measurement of this nature [cf. Eq. (13)] and was adopted to probe the energy gap between the $S = ½$ ground state and $S = {}^3/_2$ excited state as a function of magnetic field through the 10.5 T avoided crossing, proving that the associated oscillations occur coherently (see Fig. 14).

The study of relaxation in SMMs has also been investigated in applied magnetic fields using time resolved INS at the IN5 spectrometer ILL, France. The principle of this method was proven in the study on an array of aligned $Mn_{12}Ac$ single crystals [249]. In this investigation, the magnetic relaxation was probed by monitoring

changes in the population of states as a function of time via the INS intensity following a switch of field direction along the sample magnetic easy-axis. Additionally, the field dependent studies aided the identification of a minority $Mn_{12}Ac$ species present within samples (see also Sect. 2.2), providing quantification and additional explanation for the anomalous fast relaxation observed in AC susceptibility measurements [250].

4.6 Antiferromagnetic Molecular Clusters: AF Rings

The spin dynamics of AF rings with dominant nearest neighbor exchange have drawn considerable interest [251–254]. Experimental investigations have uncovered a wealth of interesting physical phenomena [255] in accordance with much of the theoretical speculation. Topics of interest include bipartite excitations [256], spin wave theory [257, 258], magnetic frustration [236, 259], and Néel vector tunneling [260, 261].

Even membered rings with nearest neighbor Heisenberg exchange have been found to follow a rotational-band-like energy dependence in accordance with the Landé interval rule [256, 262, 263]. This rule, $E_S = \Delta_0 S(S+1)/2$, gives the energy dependence of spin states with increasing S (known as the L-band), where Δ_0 is the energy gap between the ground and first excited spin state. An approximate Hamiltonian can be used to express this band of excitations, where an effective exchange (J_{eff}) between two sub-lattice spin vectors, S_A and S_B, is considered. Conformation to this bipartite model assumes collective behavior between sub-lattice spins in the absence of quantum fluctuations. Within this context the energy dependence can be considered semi-classical in nature [264], analogous to the magnetic bi-stability in SMMs. A second, higher energy band of excitations, the so-called E-band, also exhibits a parabolic energy dependence upon increasing spin, displaced in energy from the L-band of excitations. The difference between the two bands of increasing spin states reflects differences within their internal spin structure. One of the first AF rings to be studied was a polycrystalline sample of Cr_8, $[Cr_8F_8(tBuCO_2)_{16}]$ [256, 265]. The Cr_8 ring exhibits a singlet $S = 0$ ground state and, at 1.5 K, transitions to $S = 1$ excited states of the L and E bands were probed. The two bands of excitations exhibit different momentum transfer dependence, reflecting the differences in their internal structure. The effect of lowering the symmetry of the Cr_8 ring by inclusion of a diamagnetic Zn ion has also been investigated by INS, i.e., a similar Cr_8Zn ring [266]. The Zn ion breaks the translational invariance around the ring, making the L-band a worse approximation; thus, mixing of the characteristic L and E band neutron momentum transfers was observed.

Néel vector tunneling has been proposed for ring systems exhibiting bipartite properties in addition to a large axial anisotropy, where alignment of the Néel vector with the z-axis (either up, $|\uparrow\rangle$, or down, $|\downarrow\rangle$) becomes energetically favorable for sufficiently strong axial anisotropy. Many investigations have pursued the

observation of Néel vector tunneling – a coherent quantum oscillation between $|\uparrow\rangle$ and $|\downarrow\rangle$ – through the anisotropy barrier. Neutron scattering experiments have been conducted in search of this tunneling in Fe-based AF rings, exhibiting large dipolar anisotropies [260, 261, 267]. However, while parameterization of general theoretical criteria could be met [251], determination of whether the tunneling transition is a genuine combination of two Néel states remains unclear. The best evidence so far for Néel vector tunneling involves magnetic torque measurements [260].

4.7 Single Crystal ToF INS

The vast majority of ToF INS investigations on MNs have been of a polycrystalline form, where the modulus of Q is obtained from the scattering cross section. In this scenario, limited information regarding the internal spin structure of the measured MN may be extracted. This is because the polycrystalline scattering cross section depends only on distances between correlated magnetic ions, washing out the detailed information concerning the dynamic spin–spin correlations between particular pairs of spins within the studied MN. The orientation average of the so-called interference terms does provide valuable information, several examples of which have been discussed here. However, this represents only part of the potential information available in comparison to measuring the full four-dimensional $S(\boldsymbol{Q}, \omega)$ cross section [268]. In fact, such a measurement *is* possible with a single-crystal MN sample, where the Fourier components of the dynamic correlations between particular magnetic ion pairs are related to their vector separation in the scattering cross section, modulating the scattering intensity with respect to $\boldsymbol{Q}$. To gain access to such information requires the measurement of large portions of $S(\boldsymbol{Q}, \omega))$, which requires neutron detectors with position sensitivity in both the azimuthal and out of plane scattering angles. Until recently, cold source ToF INS spectrometers had just unitary detectors which measure on Debye-Scherrer rings. However, with the development of ^{3}He position sensitive detectors for cold source neutron ToF INS, the coverage of large detection solid angles, with full $S(\boldsymbol{Q}, \omega))$ analysis, is within reach [211, 212, 226, 269]. Embedded within the Fourier components of the dynamic spin correlations is detailed information regarding the low temperature dynamics. The measured correlations can be linked to the low temperature dynamics by linear response functions. These functions are represented by a set of susceptibilities, which provide the response of a spin d at time t to a magnetic field pulse vector to spin d' at time $t = 0$. Such information can provide critical information regarding the internal spin structure within a MN, enabling, e.g., a validation of the Néel vector tunneling regime within AF rings. Additionally, the sum of the full set of dynamical spin correlations gives the equal time correlation functions, which characterize the spin structure of the ground state [270].

Successful extraction of the dynamic spin pair correlations within a MN has been demonstrated in 2012 [270]. The measurements were performed on the IN5

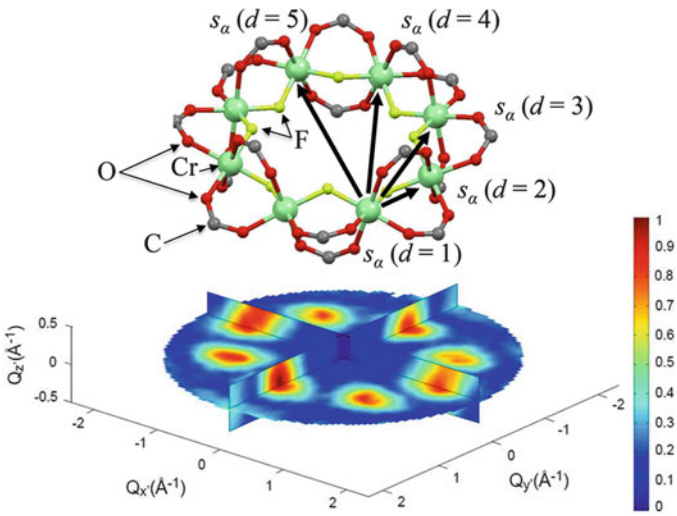

Fig. 15 (*Top*) Principal correlated spin pairs ($d=1$ to 5), with respect to vectors (*thick arrows*) within the Cr_8 MN. The Cr atom (*large balls*) pairs in the ring are bridged by fluorines and two $tBuCO_2$ groups, with carboxylates cropped for clarity (see labeling). (*Bottom*) Combined $S(\boldsymbol{Q})$ of Cr_8 for the *L*-band magnetic excitation, $p=1$. Adapted with permission from [270]. Copyright 2012 Nature Publishing Group

spectrometer following an upgrade which saw the installation of position sensitive detectors composed of 10^5 pixels covering a total of 30 m^2. A 240 mg single-crystal of the well characterized prototype AF ring Cr_8 was selected for the investigation. INS spectra were measured in one-degree steps, rotating the crystal to access a large range of momentum transfers. At 1.5 K, transitions from the $S=0$ ground state access three $S=1$ excited states labeled $p=1$, 2, and 3. The $p=1$ transition reaches into the $S=1$ first excited state (*L*-band), and $p=2$ and 3 go to $S=1$ excited states (*E*-band), while further transitions into additional excited states exhibit close to zero oscillator strength. An integrated energy cut displaying the measured neutron scattering momentum transfer for the $p=1$ transition is shown in Fig. 15. The magnetic neutron scattering cross section [Eq. (9)] for the specific case of a homometallic MN with axial anisotropy, as $T\rightarrow 0$, may be written as [206]:

$$S(\boldsymbol{Q},\omega) \propto \sum_{\alpha=x,y,z}\left(1-\frac{Q_\alpha^2}{Q^2}\right)\sum_p\sum_{d\geq d'}^{N} F_d(Q)\times F_{d'}(Q)\cos\left(\boldsymbol{Q}\cdot\boldsymbol{R}_{dd'}\right), \\ \times\left\langle 0\middle|s_\alpha(d)\middle|p\right\rangle\left\langle p\middle|s_\alpha\left(d'\right)\middle|0\right\rangle\delta\left(E_i-E_f+\hbar\omega_p\right) \tag{17}$$

where $F_d(Q)$ is the magnetic form factor of the dth ion in the ring, $\boldsymbol{R}_{dd'}$ is the vector between ion d with spin $s_\alpha(d)$ and ion d' with spin $s_\alpha(d')$, and $|0\rangle$ and $|p\rangle$ are the ground and excited eigen-functions of the magnetic transition p, with eigenvalue $\hbar\omega_p$. The $\langle 0|s_\alpha(d)|p\rangle\langle p|s_\alpha(d')|0\rangle$ terms represent the Fourier components of the

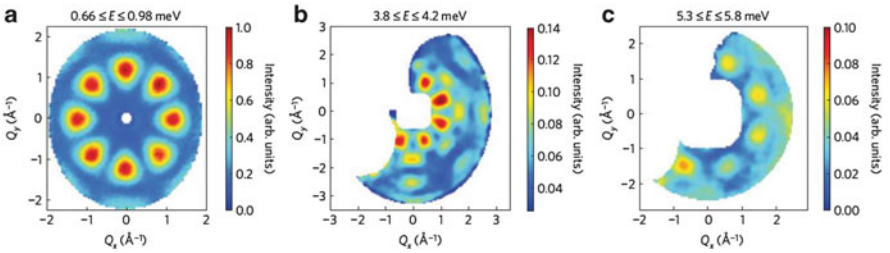

Fig. 16 Constant energy cuts for magnetic excitations $p = 1$, 2, and 3 [(**a**)–(**c**), respectively]. The maps show the Q_x–Q_y wave vector dependence lying in the plane of the Cr_8 ring. Adapted with permission from [270]. Copyright 2012 Nature Publishing Group

dynamical correlations between ions within the MN. Hence, by fitting [271] Eq. (17) to the measured $S(\boldsymbol{Q}, \omega)$ for excitations $p = 1$, 2, 3, the full set of Fourier components for the dynamical correlations may be extracted directly from the measurement without reliance on any spin Hamiltonian model. The Cr_8 molecule exhibits 5 principle correlations (see Fig. 15): the self-correlation $d = 1$, and pair correlations $d = 1$ to $2 \rightarrow 5$, where $d = 6$, 7, 8 are equivalents to $d = 4$, 3, 2, respectively. Figure 16 shows constant energy plots for the excitations $p = 1$, 2, 3, showing the momentum transfer for two wave-vector components, Q_x and Q_y, lying in the plane of the Cr_8 ring. Fits to the full three wave-vector components for each transition successfully extracted the Fourier components of the two spin dynamical correlations. The obtained values were found to correspond very well to exact values extracted from a microscopic Hamiltonian calculation solved for Cr_8 in [265].

4.8 Future Prospects

The selection of key studies reported here demonstrates that INS has played an integral role in the development of the MN research field. Today much effort goes into taking MNs out of the crystal for manipulation [272] of their quantum properties on surfaces [169] or within nanotubes [273]. However, before control of MNs can be achieved to such a precision that applications like QIP could become a reality, an extensive understanding of the structure of eigenstates within prototype clusters must be reached. The recent development of ToF INS spectrometers underpins a renaissance for the characterization of MNs, providing a way to probe detailed wave-function information for development of this research area. As exemplified in the single-crystal study of Cr_8 [270], extraction of two-spin dynamical correlations opens up new possibilities to access the internal spin structure of MNs. It will be fascinating to see the application of single crystal ToF INS to probe quantum entanglement within prototype qubits, composed of supramolecular complexes of linked MNs [274, 275]. Another field of interest

includes confirmation of Néel vector tunneling in AF rings. The extracted spin correlation information obtained from the single-crystal INS study of Cr_8 demonstrated that the degree of validity of the Néel vector tunneling framework can be tested directly.

A further instrumentation development will be the integration of large applied magnetic fields with ToF INS on single crystals of MNs. The evolution of MN cluster wave-functions with applied magnetic fields could be used to investigate quantum phenomena such as avoided spin state crossings, and the effect of magnetic fields on exchange biased qubit prototypes. Applied fields provide a means of accessing detailed information regarding the internal spin structure of the degenerate eigenstates in frustrated systems and MNs exhibiting magnetic vortex-spin chirality [276]. The Cr_8 single crystal study revealed how the propagation of quantum fluctuations can be observed. It was shown how the propagation of a local disturbance causes a wave-like motion of the magnetization around the ring, with the occurrence of constructive interference as both anti-clockwise and clockwise propagations meet at the opposite side of the ring. It will be of interest to obtain the same information for odd membered, frustrated rings [236, 277], where complex interference effects should occur as out-of-phase propagations of magnetization meet. Coupling single crystal studies with applied magnetic fields will open up further opportunities for probing elusive physical phenomena within MNs. Fields of just a couple of Tesla are enough to investigate phenomena such as entanglement or frustration-induced degeneracy; many spectrometers are already equipped and ready for such investigations.

In summary, single crystal INS changes the landscape in terms of the amount of detailed information that can be experimentally probed within MNs. The recent demonstration of this method on the prototypical AF ring, Cr_8, highlights what can be achieved. This method currently requires very large crystals – of order of 200 mg; additionally, the arrangements of molecules within the unit cell must be as simple as possible. In most cases, deuteration is required, introducing further complexity to chemical synthesis. However, it is frequently observed that incoherent scattering from hydrogen only becomes significant at energies greater than around 2 meV. The characterization of polycrystalline samples becomes an increasingly rapid method to investigate MNs, with greater energy resolutions enabling measurements of small zfs interactions. The latest cold source ToF INS spectrometers (LET and AMATERAS) present the possibility of measuring multiple dynamic ranges at the same time, known as RRM. This will enable the measurement of $S(\boldsymbol{Q}, \omega)$ over a broader dynamic range than possible with a single monochromating pulse rate, reducing the amount of time needed to obtain the three vector scattering intensities for all magnetic excitations over a broad energy range within a MN. ToF INS on single crystals of MNs represents the frontier of what is currently possible with today's neutron scattering technology. However, the construction of new neutron scattering facilities, such as the European Spallation source [278], should see increases of neutron beam intensities by many orders of magnitude, permitting the study of more complex high-nuclearity structures with much smaller crystal sizes.

5 Muon-Spin Rotation

In a μ^+SR experiment [279, 280], spin-polarized positively charged muons are stopped in a target sample. The time evolution of the muon spin polarization is probed via the positron decay asymmetry function $A(t)$ to which it is proportional. Such experiments can be carried out at muon sources which are available in various locations around the world (currently J-PARC in Japan, PSI in Switzerland, RAL in the UK, and TRIUMF in Canada). They give a means of measuring local magnetization and dynamics from the viewpoint of the implanted probe, the spin-polarized muon. A conventional magnetometry measurement of the magnetic susceptibility χ yields

$$\chi = \lim_{\delta H \to 0} \frac{\delta M_{\mathrm{av}}}{\delta H}, \tag{18}$$

where M_{av} is given by $M_{\mathrm{av}} = \frac{1}{V}\int_V M(\mathbf{r}) d^3 r$, a volume averaged magnetization. In contrast, from μ^+SR data one can extract the staggered magnetization distribution $\rho(M)$ in zero applied field; thus if there are N crystallographically independent muon sites (in most molecular magnetic materials that have been studied, it is found that N is 1, 2, or 3), such that a fraction f_i of the muons implant at the ith site, then one can assume that the measured muon polarization function $A(t)$ (neglecting weakly relaxing terms due to longitudinal relaxation) follows

$$A(t) \propto \sum_{i=1}^{N} f_i \int \rho(M) e^{-\lambda_i t} \cos\left(\alpha_i M t\right) dM, \tag{19}$$

where α_i is a constant which depends on the dipolar coupling between the local magnetization M and the muon at site i, and λ_i is a relaxation rate. If the sample has uniform staggered magnetization M_0 so that $\rho(M) = \delta(M - M_0)$, then

$$A(t) \propto \sum_{i=1}^{N} f_i e^{-\lambda_i t} \cos\left(\alpha_i M_0 t\right). \tag{20}$$

Muons can hence allow the temperature dependence of M_0 to be determined and have the useful advantage that they can demonstrate rather easily that M_0 is a characteristic of the entirety of the sample, and not of a minority impurity phase.

5.1 Applications of μ^+*SR*

Muons have a particular advantage in the case of low-dimensional magnets [281–283]. Because the correlation length ξ in an antiferromagnetic chain grows on cooling, the heat capacity exhibits a rather broad maximum as the entropy of the

spins consequently decreases with the increasing correlation. Thus, when 3D ordering sets in at T_N, the transition is associated only with a rather small change in entropy, thereby giving rise to a tiny peak in the heat capacity, the size of which decreases as $|J'/J|$ decreases. This effect is shown in recent Monte Carlo simulations for quasi-two-dimensional systems [284], and means that identifying 3D ordering in very anisotropic magnets using heat capacity can be challenging. In contrast, the transition from a non-long-range ordered state, even one with dynamic correlations of large spatial extent, to a 3D long-range ordered state is rather straightforward using μ^+SR [282].

However, for MNs, measurements made using μ^+SR have proven difficult to interpret, and the large number of muon sites within a complex molecule that will inevitably occur do not make the situation easy. Although initially it was thought that QTM should be measurable by implanting muons into MNs [285–287], the unambiguous detection of this effect proved elusive [288]. Instead, μ^+SR spectra obtained on high spin systems appeared to arise from dynamic fluctuations of a local magnetic field distribution at the muon sites, which persisted down to dilution refrigerator temperatures [286–289]. Muon results on MN systems all showed similar behavior but it was unclear whether the muon was probing the intrinsic behavior of the large electronic spin or some residual effect. It has been argued that μ^+SR is sensitive to the dephasing of the MN electronic spins caused by the incoherent fluctuations of nuclear moments in which the metal ions are embedded [290]. If this is the case then it makes the muon a valuable probe of the potential mechanism behind QTM. In order to address the question of what the muon probes in MN systems, identical μ^+SR measurements were performed [291] on protonated and deuterated samples of Cr_7Mn ($S = 1$) and Cr_8 ($S = 0$) [292, 293] [structure shown in the inset of Fig. 17a, b]. These measurements show (1) that the muon is controlled by the large electronic spin in a MN; (2) deuteration leads to a significant increase in the μ^+SR relaxation rate at low temperature in Cr_7Mn, implying that muons probe the dephasing of large electronic spins by the random magnetic fields due to the nuclei and; (3) that upon cooling, a magnetic ground state is reached by a freezing out of dynamic processes that leads to magnetic order in Cr_7Mn below 2 K [291]. Typical spectra measured for Cr_7Mn and Cr_8 are shown in Fig. 17. Above $T \approx 2$ K the spectra for all materials differ depending on whether protonated or deuterated.

In the temperature range $2 \leq T \leq 100$ K the spectra for $S = 1$ Cr_7Mn (Fig. 17a) were found to be described by the relaxation function $A(t) = A_1 \exp\left(-\sqrt{\lambda t}\right) + A_{bg}$; where A_{bg} accounts for any background contribution from muons that stop in the sample holder or cryostat tails. This behavior is typical of that observed previously in MN materials [286, 287, 290] and arises because of the complex dynamic distribution of local fields within the material sampled by the muon ensemble. The monotonic relaxation and the fact that the muons could not be decoupled with an applied magnetic field up to 0.6 T places the relaxation in the fast-fluctuation limit [294]. The spectra measured for the $S = 0$ Cr_8 samples are quite different (Fig. 17b). In this case the relaxation rate is far smaller and resembles a Kubo-Toyabe (KT) function with a distribution width given by $\Delta = \gamma_\mu \langle B^2 \rangle^{1/2}$, where

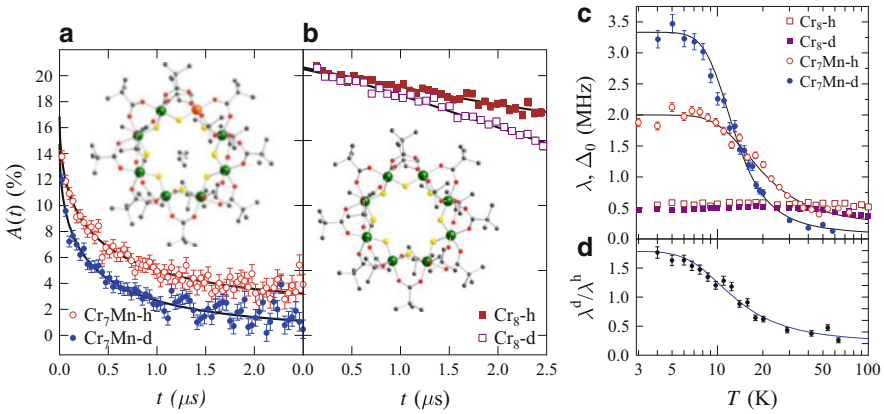

Fig. 17 Spectra for protonated and deuterated Cr_7Mn (**a**) and Cr_8 (**b**) materials, measured at $T = 4.5$ K. *Insets*: structures of the molecules. (**c**) Temperature evolution of the relaxation rates. (**d**) Ratio of the Cr_7Mn-h and -d relaxation rates. The *line* is a guide to the eye. Adapted with permission from [291]. Copyright 2010 American Physical Society

$\gamma_\mu = 2\pi \times 135.5$ MHz T^{-1} is the muon gyromagnetic ratio and B is the local magnetic field at a muon site [294]. In a MN there are many inequivalent classes of muon sites and this leads to a distribution of second moments $p(\Delta)$. The resulting muon relaxation is obtained by averaging the KT function over this distribution, and an analysis [291] shows that the muon is sensitive to the disordered nuclear moments in Cr_8. This is confirmed by the application of a small longitudinal magnetic field which quenches the relaxation. The larger Δ found in Cr_8-d compared to Cr_8-h reflects (albeit partially) the larger moment of the deuteron. Most importantly, the dramatic difference between the measured spectra and relaxation rates for $S = 0$ Cr_8 and $S = 1$ Cr_7Mn samples (Fig. 17a, b) strongly suggests that the muon response in MN systems with $S \neq 0$ stems from dynamic fluctuations of the *electronic* spin. In the absence of an electron spin in Cr_8, the muon spin is relaxed by quasistatic disordered nuclear moments.

The temperature dependence of the relaxation rate λ for the protonated (λ^h) and deuterated (λ^d) Cr_7Mn samples is shown in Fig. 17c. On cooling below $T \sim 50$ K, the relaxation rate λ increases before saturating below ~10 K, with the onset of the increase and the saturation occurring at similar values of T for both materials. This T-dependence is common to nearly all MN systems that have been previously measured with μ^+SR [286–288, 290] and is discussed in more detail below. At high temperature $\lambda^d > \lambda^h$. It is likely that at these high temperatures the electronic spins are fluctuating very fast and are at least partially motionally narrowed from the spectra. Upon cooling, the increase in λ is greater for the deuterated sample, with λ^d becoming greater than λ^h below $\approx$15 K. Most significantly, the saturation of the relaxation at $T \lesssim 10$ K occurs with $\lambda^d > \lambda^h$. The temperature dependence of the ratio λ^d/λ^h (Fig. 17d), which increases upon cooling, tends to $\approx$1.7 at the lowest temperature.

The muon relaxation rate is proportional to the electronic spin correlation time τ_e and $1/\tau_e \propto \langle B_n{}^2 \rangle \tau_n$, where τ_n is the correlation time of the nuclear stochastic field. It is probable that swapping protons for deuterons changes not only the local field distribution (via $\langle B_n{}^2 \rangle$) but also the correlation time of the nuclear stochastic field [291].

Measurements made down to 20 mK show heavily damped oscillations which are identical for -h and -d samples and lead to an estimate of a transition temperature of 1.9(1) K to a state of magnetic order. The heavily damped nature of the oscillations and the Cr_8 results suggest that there are many magnetically inequivalent muon sites in the system. μ^+SR is likely to be particularly effective in revealing transitions to long-range order in MNs and this is a fruitful area for future research. A second interesting topic is the recent observation using muons of electronic energy level crossings [295]. This gives further evidence that the spin relaxation of the implanted muon is sensitive to the dynamics of the electronic spin. The experiment was performed on a broken ring MN Cr_8Cd and the data show clear evidence for the $S = 0$ to $S = 1$ transition that takes place at $B_c = 2.3$ T. The crossing is observed as a resonance-like dip in the average positron asymmetry and also in the muon spin relaxation rate, which shows a sharp increase in magnitude at the transition and a peak centered within the $S = 1$ regime [295]. A third interesting new direction concerns the study of MNs on surfaces using the technique of proximal magnetometry [296] in which very low energy muons are used as a spin probe, implanting them in the substrate, just below the magnetic material. Such experiments are beginning to bear fruit [297].

Acknowledgements All of the authors are indebted to collaborators whose names can be found in a number of the references cited. MLB would especially like to thank Hannu Mutka, Hans-Uli Güdel, Tatiana Guidi, Stefano Carretta, and Paolo Santini; his recent research position is supported by the Army Research Office (W911NF-13-1-0125). SJB would like to thank Tom Lancaster, Francis Pratt, Richard Winpenny and Arzhang Ardavan; his research is supported by EPSRC and STFC (UK). ND acknowledges the Ministerio de Ciencia e Innovación of Spain for a grant under the program Ramón y Cajal. SH would like to acknowledge the NSF (DMR 1309463) and the Air Force (AOARD grant #134031) for financial support. Work at the NHMFL is supported by the NSF (DMR 1157490) and the State of Florida.

References

1. Caneschi A, Gatteschi D, Sessoli R, Barra AL, Brunel LC, Guillot M (1991) J Am Chem Soc 113:5873
2. Brunel L-C, van Tol J, Angerhofer A, Hill S, Krzystek J, Maniero AL (2004) In: Grinberg O, Berliner LJ (eds) Very high frequency EPR, vol 22, Biological magnetic resonance. Springer, New York, p 465
3. Barra AL, Gatteschi D, Sessoli R (1997) Phys Rev B 56:8192
4. Hill S, Perenboom JA, Dalal NS, Hathaway T, Stalcup T, Brooks JS (1998) Phys Rev Lett 80:2453
5. Barra A-L, Debrunner P, Gatteschi D, Schulz CE, Sessoli R (1996) Europhys Lett 35:133
6. Dobrovitski VV, Katsnelson MI, Harmon BN (2000) Phys Rev Lett 84:3458

7. Leuenberger MN, Loss D (2001) Nature 410:789
8. Lehmann J, Gaita-Ariño A, Coronado E, Loss D (2007) Nat Nanotechnol 2:312
9. Lehmann J, Gaita-Ariño A, Coronado E, Loss D (2009) J Mater Chem 19:1672
10. Troiani F, Bellini V, Candini A, Lorusso G, Affronte M (2010) Nanotechnology 21:274009
11. Rudowicz C, Misra SK (2001) Appl Spectrosc Rev 36:11
12. Liu J, del Barco E, Hill S (2014) In: Bartolomé J, Luis F, Fernández J (eds) Molecular magnets: physics and applications, Springer series on nanoscience and technology. Springer, Berlin, pp 77–110
13. Lampropoulos C, Murugesu M, Harter AG, Wernsdofer W, Hill S, Dalal NS, Abboud KA, Christou G (2013) Inorg Chem 52:258
14. Barra A-L, Goiran M, Sessoli R, Zvyagin SA (2013) C R Phys 14:106
15. Hassan AK, Pardi LA, Krzystek J, Sienkiewicz A, Goy P, Rohrer M, Brunel LC (2000) J Magn Reson 142:300
16. Mola M, Hill S, Goy P, Gross M (2000) Rev Sci Instrum 71:186
17. Schnegg A, Behrends J, Lips K, Bittl R, Holldack K (2009) Phys Chem Chem Phys 11:6820
18. Hill S (2013) Polyhedron 64:128
19. Zadrozny JM, Xiao DJ, Atanasov M, Long GJ, Grandjean F, Neese F, Long JR (2013) Nat Chem 5:577
20. Sessoli R, Tsai H-L, Schake AR, Wang S, Vincent JB, Folting K, Gatteschi D, Christou G, Hendrickson DN (1993) J Am Chem Soc 115:1804
21. Sessoli R, Gatteschi D, Caneschi A, Novak M (1993) Nature 365:141
22. Redler G, Lampropoulos C, Datta S, Koo C, Stamatatos TC, Chakov NE, Christou G, Hill S (2009) Phys Rev B 80:094408
23. Petukhov K, Hill S, Chakov NE, Christou G (2004) Phys Rev B 70:054426
24. Hill S, Anderson N, Wilson A, Takahashi S, Petukhov K, Chakov NE, Murugesu M, North JM, del Barco E, Kent AD, Dalal NS, Christou G (2005) Polyhedron 24:2284
25. Hill S, Anderson N, Wilson A, Takahashi S, Chakov NE, Murugesu M, North JM, Dalal NS, Christou G (2005) J Appl Phys 97:10M510
26. Chakov NE, Lee S-C, Harter AG, Kuhns PL, Reyes AP, Hill SO, Dalal NS, Wernsdorfer W, Abboud KA, Christou G (2006) J Am Chem Soc 128:6975
27. Rudowicz C, Chung CY (2004) J Phys Condens Matter 16:5825
28. Stoll S, Schweiger A (2006) J Magn Reson 178:42
29. Friedman JR, Sarachik MP, Tejada J, Ziolo R (1996) Phys Rev Lett 76:3830
30. Thomas L, Lionti F, Ballou R, Gatteschi D, Sessoli R, Barbara B (1996) Nature 383:145
31. Wernsdorfer W, Sessoli R (1999) Science 284:133
32. del Barco E, Kent AD, Hill S, North JM, Dalal NS, Rumberger EM, Hendrickson DN, Chakov N, Christou G (2005) J Low Temp Phys 140:119
33. Takahashi S, Edwards RS, North JM, Hill S, Dalal NS (2004) Phys Rev B 70:094429
34. Hill S, Edwards RS, Jones SI, North JM, Dalal NS (2003) Phys Rev Lett 90:217204
35. Wilson A, Lawrence J, Yang E-C, Nakano M, Hendrickson DN, Hill S (2006) Phys Rev B 74, R140403
36. Kirman C, Lawrence J, Hill S, Yang E-C, Hendrickson DN (2005) J Appl Phys 97:10M501
37. Lawrence J, Hill S, Yang E-C, Hendrickson DN (2009) Phys Chem Chem Phys 2009:6743
38. Hill S, Murugesu M, Christou G (2009) Phys Rev B 80:174416
39. Barra A-L, Caneschi A, Cornia A, Gatteschi D, Gorini L, Heiniger L-P, Sessoli R, Sorace L (2007) J Am Chem Soc 129:10754
40. Sorace L, Boulon M-E, Totaro P, Cornia A, Fernandes-Soares J, Sessoli R (2013) Phys Rev B 88:104407
41. Lawrence J, Yang E-C, Edwards R, Olmstead MM, Ramsey C, Dalal NS, Gantzel PK, Hill S, Hendrickson DN (2008) Inorg Chem 47:1965
42. Cornia A, Sessoli R, Sorace L, Gatteschi D, Barra AL, Daiguebonne C (2002) Phys Rev Lett 89:257201
43. Bircher R, Chaboussant G, Sieber A, Güdel HU, Mutka H (2004) Phys Rev B 70:212413

44. del Barco E, Kent AD, Rumberger EM, Hendrickson DN, Christou G (2003) Phys Rev Lett 91:047203
45. Parks B, Loomis J, Rumberger E, Hendrickson DN, Christou G (2001) Phys Rev B 64:184426
46. Macia F, Lawrence J, Hill S, Hernandez JM, Tejada J, Santos PV, Lampropoulos C, Christou G (2008) Phys Rev B 77:020403(R)
47. van Slageren J, Vongtragool S, Gorshunov B, Mukhin A, Dressel M (2009) Phys Rev B79:224406
48. Wernsdorfer W, Sessoli R, Gatteschi D (1999) Europhys Lett 47:254
49. Maccagnano S, Achey R, Negusse E, Lussier A, Mola MM, Hill S, Dalal NS (2001) Polyhedron 20:1441
50. Park K, Novotny MA, Dalal NS, Hill S, Rikvold PA (2001) Phys Rev B 65:014426
51. Park K, Novotny MA, Dalal NS, Hill S, Rikvold PA (2002) Phys Rev B 66:144409
52. Hill S, Maccagnano S, Park K, Achey RM, North JM, Dalal NS (2002) Phys Rev B 65:224410
53. Takeda K, Awaga K, Inabe T, Yamaguchi A, Ishimoto H, Tomita T, Mitamura H, Goto T, Mori N, Nojiri H (2002) Phys Rev B 65:094424
54. Vongtragool S, Mukhin A, Gorshunov B, Dressel M (2004) Phys Rev B 69:104410
55. van Slageren J, Vongtragool S, Mukhin A, Gorshunov B, Dresses M (2005) Phys Rev B 72:020401
56. El Hallak F, van Slageren J, Gómez-Segura J, Ruiz-Molina D, Dressel M (2007) Phys Rev B 75:104403
57. Carbonera C, Luis F, Campo J, Sánchez-Marcos J, Camón A, Chaboy J, Ruiz-Molina D, Imaz I, van Slageren J, Dengler S, González M (2010) Phys Rev B 81:014427
58. Chudnovsky EM, Garanin DA (2001) Phys Rev Lett 87:187203
59. Mertes KM, Suzuki Y, Sarachik MP, Paltiel Y, Shtrikman H, Zeldov E, Rumberger E, Hendrickson DN, Christou G (2001) Phys Rev Lett 87:227205
60. Garanin DA, Chudnovsky EM (2002) Phys Rev B 65:094423
61. Wen B, Subedi P, Bo L, Yeshurun Y, Sarachik MP, Kent AD, Millis AJ, Lampropoulos C, Christou G (2010) Phys Rev B 82:014406
62. Burzurí E, Carbonera C, Luis F, Ruiz-Molina D, Lampropoulos C, Christou G (2009) Phys Rev B 80:224428
63. Sessoli R, Gatteschi D, Caneschi A, Novak M (1993) Nature 365:141
64. Wernsdorfer W, Chakov NE, Christou G. arXiv:cond-mat/0405014v2 (unpublished)
65. Soler M, Wernsdorfer W, Sun Z, Huffman JC, Hendrickson DN, Christou G (2003) Chem Commun 2003:2672
66. Lampropoulos C, Redler G, Data S, Abboud KA, Hill S, Christou G (2010) Inorg Chem 49:1325
67. Bagai R, Christou G (2009) Chem Soc Rev 38:1011
68. del Barco E, Kent AD, Chakov NE, Zakharov LN, Rheingold AL, Hendrickson DN, Christou G (2004) Phys Rev B 69:020411
69. van Slageren J, Vongtragool S, Gorshunov B, Mukhin AA, Karl N, Krzystek J, Telser J, Müller A, Sangregorio C, Gatteschi D, Dressel M (2003) Phys Chem Chem Phys 5:3837
70. Prokof'ev NV, Stamp PCE (1998) Phys Rev Lett 80:5794
71. Liu J, Beedle CC, Quddusi HM, del Barco E, Hendrickson DN, Hill S (2011) Polyhedron 30:2965
72. Ferguson A, Lawrence J, Parkin A, Sanchez-Benitez J, Kamanev KV, Brechin EK, Wernsdorfer W, Hill S, Murrie M (2008) Dalton Trans 2008:6409
73. Feng PL, Koo C, Henderson JJ, Nakano M, Hill S, del Barco E, Hendrickson DN (2008) Inorg Chem 47:8610
74. Feng PL, Koo C, Henderson J, Manning P, Nakano M, del Barco E, Hill S, Hendrickson DN (2009) Inorg Chem 48:3480

75. Henderson JJ, Koo C, Feng PL, del Barco E, Hill S, Tupitsyn IS, Stamp PCE, Hendrickson DN (2009) Phys Rev Lett 103:017202
76. Hill S, Datta S, Liu J, Inglis R, Milios CJ, Feng PL, Henderson JJ, del Barco E, Brechin EK, Hendrickson DN (2010) Dalton Trans 39:4693
77. Liu J, del Barco E, Hill S (2012) Phys Rev B 85:014206
78. Quddusi HM, Liu J, Singh S, Heroux KJ, del Barco E, Hill S, Hendrickson DN (2011) Phys Rev Lett 106:227201
79. Heroux KJ, Quddusi HM, Liu J, O'Brien JR, Nakano M, del Barco E, Hill S, Hendrickson DN (2011) Inorg Chem 50:7367
80. Stoll S, Shafaat HS, Krzystek J, Ozarowski A, Tauber MJ, Kim JE, Britt RD (2011) J Am Chem Soc 133:18098
81. Datta S, Waldmann O, Kent AD, Milway VA, Thompson LK, Hill S (2007) Phys Rev B 76:052407
82. Bencini A, Ciofini I, Uytterhoeven MG (1998) Inorg Chim Acta 274:90
83. Yang E-C, Kirman C, Lawrence J, Zakharov LN, Rheingold AL, Hill S, Hendrickson DN (2005) Inorg Chem 44:3827
84. Datta S, Bolin E, Inglis R, Milios CJ, Brechin EK, Hill S (2009) Polyhedron 28:1911
85. Hill S, Edwards RS, Aliaga-Alcalde N, Christou G (2003) Science 302:1015
86. Liu J, Koo C, Amjad A, Feng PL, Choi E-S, del Barco E, Hendrickson DN, Hill S (2011) Phys Rev B 84:094443
87. Liu J, Hill S (2013) Polyhedron 66:147
88. Ako AM, Hewitt IJ, Mereacre V, Clerac R, Wernsdorfer W, Anson CE, Powell AK (2006) Angew Chem Int Ed 45:4926
89. Milios CJ, Vinslava A, Wernsdorfer W, Moggach S, Parsons S, Perlepes SP, Christou G, Brechin EK (2007) J Am Chem Soc 129:2754
90. Inglis R, Taylor SM, Jones LF, Papaefstathiou GS, Perlepes SP, Datta S, Hill S, Wernsdorfer W, Brechin EK (2009) Dalton Trans 2009:9157
91. Inglis R, Jones LF, Milios CJ, Datta S, Collins A, Parsons S, Wernsdorfer W, Hill S, Perlepes SP, Piligkos S, Brechin EK (2009) Dalton Trans 2009:3403
92. Waldmann O (2007) Inorg Chem 46:10035
93. Harman WH, Harris TD, Freedman DE, Fong H, Chang A, Rinehart JD, Ozarowski A, Sougrati MT, Grandjean F, Long GJ, Long JR, Chang CJ (2010) J Am Chem Soc 132:18115
94. Zadrozny JM, Atanasov M, Bryan AM, Lin C-Y, Rekken BD, Power PP, Neese F, Long JR (2013) Chem Sci 4:125
95. Lawrence J, Beedle C, Ma J, Hill S, Hendrickson DN (2007) Polyhedron 26:2299
96. Liu J, Datta S, Bolin E, Lawrence J, Beedle CC, Yang E-C, Goy P, Hendrickson DN, Hill S (2009) Polyhedron 28:1922
97. Zadrozny JM, Liu J, Piro NA, Chang CJ, Hill S, Long JR (2012) Chem Commun 48:3927
98. Ruamps R, Maurice R, Batchelor L, Boggio-Pasqual M, Guillot R, Barra A-L, Liu J, Bendief E-E, Pillet S, Hill S, Mallah T, Guihery N (2013) J Am Chem Soc 135:3017
99. Ishikawa N, Sugita M, Ishikawa T, Koshihara S, Kaizu Y (2003) J Am Chem Soc 125:8694
100. Ishikawa N, Sugita M, Wernsdorfer W (2005) J Am Chem Soc 127:3650
101. AlDamen MA, Clemente-Juan JM, Coronado E, Martí-Gustaldo C, Gaita-Ariño A (2008) J Am Chem Soc 130:8874
102. Ghosh S, Datta S, Friend L, Cardona-Serra S, Coronado E, Hill S (2012) Dalton Trans 41:13697
103. Tang J, Hewitt I, Madhu NT, Chastanet G, Wernsdorfer W, Anson CE, Benelli C, Sessoli R, Powell AK (2006) Angew Chem Int Ed 45:1729
104. Long J, Habib F, Lin PH, Korobkov I, Enright G, Ungur L, Wernsdorfer W, Chibotaru LF, Murugesu M (2011) J Am Chem Soc 133:5319
105. Rinehart JD, Fang M, Evans WJ, Long JR (2011) Nat Chem 3:538
106. Rinehart JD, Fang M, Evans WJ, Long JR (2011) J Am Chem Soc 133:14236

107. Mills DP, Moro F, McMaster J, van Slageren J, Lewis W, Blake AJ, Liddle ST (2011) Nat Chem 3:454
108. Dreiser J, Schnegg A, Holldack K, Pedersen KS, Schau-Magnussen M, Nehrkorn J, Tregenna-Piggott P, Mutka H, Weihe H, Bendix J, Waldmann O (2011) Chem Eur J 17:7492
109. Telser J, van Slageren J, Vongtragool S, Dressel M, Reiff WM, Zvyagin SA, Ozarowski A, Krzystek J (2005) Magn Reson Chem 43:S130
110. Rebilly J-N, Charron G, Rivière E, Guillot R, Barra A-L, Durán Serrano M, van Slageren J, Mallah T (2008) Chem Eur J 14:1169
111. Ray K, Begum A, Weyhermüller T, Piligkos S, van Slageren J, Neese F, Wieghardt K (2005) J Am Chem Soc 127:4403
112. Forshaw AP, Smith JM, Ozarowski A, Krzystek J, Smirnov D, Zvyagin SA, Harris TD, Karunadasa HI, Zadrozny JM, Schnegg A, Holldack K, Jackson TA, Alamiri A, Barnes DM, Telser J (2013) Inorg Chem 52:144
113. Feng X, Liu J, Harris TD, Hill S, Long JR (2012) J Am Chem Soc 134:7521
114. Takahashi S, Hill S (2005) Rev Sci Instrum 76:023114
115. Brooks JS, Crow JE, Moulton WG (1998) J Phys Chem Solids 59:569
116. Zvyagin SA, Ozerov M, Cizmar E, Kamenskyi D, Zherlitsyn S, Heransdorfer T, Woznitsa J, Wunsch R, Seidel W (2009) Rev Sci Instrum 80:073102
117. Schweiger A, Jeschke G (2001) Principles of pulse electron paramagnetic resonance. Oxford University Press, New York
118. Morley GW, Brunel L-C, van Tol J (2005) Rev Sci Instrum 79:064703
119. Hofbauer W, Earle KA, Dunnam CR, Moscicki JK, Freed JH (2004) Rev Sci Instrum 75:1194
120. Cruikshank PAS, Bolton DR, Robertson DA, Hunter RI, Wylde RJ, Smith GM (2009) Rev Sci Instrum 80:103102
121. Takahashi S, Hanson R, van Tol J, Sherwin M, Awschalom D (2008) Phys Rev Lett 101:047601
122. Thomann H, Morgan TV, Jin H, Burgmayer SJN, Bare RE, Stiefel EI (1987) J Am Chem Soc 109:7913
123. Britt RD, Zimmermann J-L, Sauer K, Klein MP (1989) J Am Chem Soc 111:3522
124. Hagen WR, van den Berg WAM, van Dongen WMAM, Reijerse EJ, van Kan PJM (1998) J Chem Soc Faraday Trans 94:2969
125. Milov AD, Maryasov AG, Tsvetkov YD (1998) Appl Magn Reson 15:107
126. Huber M, Lindgren M, Hammarstrom P, Martensson LG, Carlsson U, Eaton GR, Eaton SS (2001) Biophys Chem 94:245
127. Borbat PP, Davis JH, Butcher SE, Freed JH (2004) J Am Chem Soc 126:7764
128. Ardavan A, Rival O, Morton JL, Blundell SJ, Tyryshkin AM, Timco GA, Winpenny REP (2007) Phys Rev Lett 98:057201
129. Wernsdorfer W (2007) Nat Mater 6:174
130. Wedge CJ, Timco GA, Spielberg ET, George RE, Tuna F, Rigby S, McInnes EJL, Winpenny REP, Blundell SJ, Ardavan A (2012) Phys Rev Lett 108:107204
131. Bellini V, Lorusso G, Candini A, Wernsdorfer W, Faust TB, Timco GA, Winpenny REP, Affronte M (2011) Phys Rev Lett 106:227205
132. Mitrikas G, Sanakis Y, Raptopoulou CP, Kordas G, Papavassiliou G (2008) Phys Chem Chem Phys 10:743
133. Bertaina S, Gambarelli S, Mitra T, Tsukerblat B, Müller A, Barbara B (2010) Nature 453:1006
134. Winpenny REP (2008) Angew Chem 47:7992
135. Bertaina S, Gambarelli S, Mitra T, Tsukerblat B, Müller A, Barbara B (2008) Nature 466:203
136. Shim JH, Bertaina S, Gambarelli S, Mitra T, Müller A, Baibekov EI, Malkin BZ, Tsukerblat B, Barbara B (2012) Phys Rev Lett 109:050401
137. Yang J, Wang Y, Wang Z, Rong X, Duan C-K, Su J-H, Du J (2012) Phys Rev Lett 108:230501

138. Schlegel C, van Slageren J, Manoli M, Brechin EK, Dressel M (2008) Phys Rev Lett 101:147203
139. Takahashi S, van Tol J, Beedle CC, Hendrickson DN, Brunel L-C, Sherwin MS (2009) Phys Rev Lett 102:087603
140. Takahashi S, Tupitsyn IS, van Tol J, Beedle CC, Hendrickson DN, Stamp PCE (2011) Nature 476:76
141. Wang Z, Datta S, Papatriantafyllopoulou C, Christou G, Dalal NS, van Tol J, Hill S (2011) Polyhedron 30:3193
142. Vergnani L, Barra A-L, Neugebauer P, Rodriguez-Douton MJ, Sessoli R, Sorace L, Wernsdorfer W, Cornia A (2012) Chem Eur J 18:3390
143. Moro F, Kaminski D, Tuna F, Whitehead GF, Timco GA, Collison D, Winpenny REP, Ardavan A, McInnes EJL (2014) Chem Commun 50:91
144. Bertaina S, Gambarelli S, Tkachuk A, Kurkin IN, Malkin B, Stepanov A, Barbara B (2007) Nat Nanotechnol 2:39
145. Martínez-Perez MJ, Cardona-Serra S, Schlegel C, Moro F, Alonso PJ, Prima-García H, Clemente-Juan JM, Evangelisti M, Gaita-Ariño A, Sesé J, van Slageren J, Coronado E, Luis F (2012) Phys Rev Lett 108:247213
146. Baldoví JJ, Cardona-Serra S, Clemente-Juan JM, Coronado E, Gaita-Ariño A, Prima-García H (2013) Chem Commun 49:8922
147. Fronk M, Bräuer B, Kortus J, Schmidt OG, Zahn DRT, Salvan G (2009) Phys Rev B 79:235305
148. Bräuer B, Fronk M, Lehmann D, Zahn DRT, Salvan G (2009) J Phys Chem B 113:14957
149. Ishii K, Ozawa K (2009) J Phys Chem C 113:18897
150. Cheesman MR, Oganesyan VS, Sessoli R, Gatteschi D, Thomson AJ (1997) Chem Commun 1997:1677
151. Domingo N, Williamson BE, Gómez-Segura J, Gerbier P, Ruiz-Molina D, Amabilino DB, Veciana J, Tejada J (2004) Phys Rev B 69:052405
152. McInnes EJL, Pidcock E, Oganesyan VS, Cheesman MR, Powell AK, Thomson AJ (2002) J Am Chem Soc 124:9219
153. Gonidec M, Davies ES, McMaster J, Amabilino DB, Veciana J (2010) J Am Chem Soc 132:1756
154. Moro F, Piga F, Krivokapic I, Burgess A, Lewis W, McMaster J, van Slageren J (2010) Inorg Chim Acta 363:4329
155. Bogani L, Cavigli L, Gurioli M, Novak RL, Mannini M, Caneschi A, Pineider F, Sessoli R, Clemente-León M, Coronado E, Cornia A, Gatteschi D (2007) Adv Mater 19:3906
156. Moroni R, Buzio R, Chincarini A, Valbusa U, de Mongeot FB, Bogani L, Caneschi A, Sessoli R, Cavigli L, Gurioli M (2008) J Mater Chem 18:109
157. Novak RL, Pineider F, de Julián Fernández C, Gorini L, Bogani L, Danieli C, Cavigli L, Cornia A, Sessoli R (2008) Inorg Chim Acta 361:3970
158. Piligkos S, Slep LD, Weyhermüller T, Chaudhuri P, Bill E, Neese F (2009) Coord Chem Rev 253:2352
159. da Cunha TT, Jung J, Boulon M-E, Campo G, Pointillart F, Pereira CLM, Le Guennic B, Cador O, Bernot K, Pineider F, Golhen S, Ouahab L (2013) J Am Chem Soc 135:16332
160. Gonidec M, Krivokapic I, Vidal-Gancedo J, Davies ES, McMaster J, Gorun SM, Veciana J (2013) Inorg Chem 52:4464
161. Malavolti L, Mannini M, Car P-E, Campo G, Pineider F, Sessoli R (2013) J Mater Chem C 1:2935
162. Collison D, Oganesyan VS, Piligkos S, Thomson AJ, Winpenny REP, McInnes EJL (2003) J Am Chem Soc 125:1168
163. Bradley JM, Thomson AJ, McInnes EJL, Winpenny REP, Timco G (2008) Dalton Trans 2008:3311
164. Bradley JM, Thomson AJ, Inglis R, Milios CJ, Brechin EK, Piligkos S (2010) Dalton Trans 39:9904

165. van Slageren J, Piligkos S, Neese F (2010) Dalton Trans 39:4999
166. Donnio B, Rivière E, Terazzi E, Voirin E, Aronica C, Chastanet G, Luneau D, Rogez G, Scheurer F, Joly L, Kappler JP, Gallani JL (2010) Solid State Sci 12:1307
167. Grumbach N, Barla A, Joly L, Donnio B, Rogez G, Terazzi E, Kappler JP, Gallani JL (2010) Eur Phys J B 73:103
168. Gambardella P, Stepanow S, Dmitriev A, Honolka J, de Groot FMF, Lingenfelder M, Gupta SS, Sarma DD, Bencok P, Stanescu S, Clair S, Pons S, Lin N, Seitsonen AP, Brune H, Barth JV, Kern K (2009) Nat Mater 8:189
169. Cornia A, Mannini M, Sainctavit P, Sessoli R (2011) Chem Soc Rev 40:3076
170. Mannini M, Sainctavit P, Sessoli R, Cartier dit Moulin C, Pineider F, Arrio M-A, Cornia A, Gatteschi D (2008) Chem Eur J 14:7530
171. Domingo N, Bellido E, Ruiz-Molina D (2012) Chem Soc Rev 41:258
172. Mannini M, Pineider F, Sainctavit P, Danieli C, Otero E, Sciancalepore C, Talarico AM, Arrio M-A, Cornia A, Gatteschi D, Sessoli R (2009) Nat Mater 8:194
173. Mannini M, Pineider F, Sainctavit P, Joly L, Fraile-Rodríguez A, Arrio M-A, Moulin CCD, Wernsdorfer W, Cornia A, Gatteschi D, Sessoli R (2009) Adv Mater 21:167
174. Mannini M, Pineider F, Sainctavit P, Cartier dit Moulin C, Arrio M-A, Cornia A, Gatteschi D, Sessoli R (2009) Eur Phys J Spec Top 169:167
175. Pineider F, Mannini M, Danieli C, Armelao L, Piras FM, Magnani A, Cornia A, Sessoli R (2010) J Mater Chem 20:187
176. Rodriguez-Douton MJ, Mannini M, Armelao L, Barra A-L, Tancini E, Sessoli R, Cornia A (2011) Chem Commun 47:1467
177. Mannini M, Tancini E, Sorace L, Sainctavit P, Arrio M-A, Qian Y, Otero E, Chiappe D, Margheriti L, Cezar JC, Sessoli R, Cornia A (2011) Inorg Chem 50:2911
178. Tancini E, Mannini M, Sainctavit P, Otero E, Sessoli R, Cornia A (2013) Chem Eur J 19:16902
179. Corradini V, Moro F, Biagi R, De Renzi V, del Pennino U, Bellini V, Carretta S, Santini P, Milway VA, Timco G, Winpenny REP, Affronte M (2009) Phys Rev B 79:144419
180. Corradini V, Ghirri A, Pennino UD, Biagi R, Milway VA, Timco G, Tuna F, Winpenny REP, Affronte M (2010) Dalton Trans 39:4928
181. Ghirri A, Corradini V, Bellini V, Biagi R, del Pennino U, De Renzi V, Cezar JC, Muryn CA, Timco GA, Winpenny REP, Affronte M (2011) ACS Nano 5:7090
182. Corradini V, Ghirri A, Garlatti E, Biagi R, De Renzi V, del Pennino U, Bellini V, Carretta S, Santini P, Timco G, Winpenny REP, Affronte M (2012) Adv Funct Mater 22:3706
183. Westerström R, Dreiser J, Piamonteze C, Muntwiler M, Weyeneth S, Brune H, Rusponi S, Nolting F, Popov A, Yang S, Dunsch L, Greber T (2012) J Am Chem Soc 134:9840
184. Stepanow S, Honolka J, Gambardella P, Vitali L, Abdurakhmanova N, Tseng T-C, Rauschenbach S, Tait SL, Sessi V, Klyatskaya S, Ruben M, Kern K (2010) J Am Chem Soc 132:11900
185. Margheriti L, Chiappe D, Mannini M, Car PE, Sainctavit P, Arrio M-A, de Mongeot FB, Cezar JC, Piras FM, Magnani A, Otero E, Caneschi A, Sessoli R (2010) Adv Mater 22:5488
186. Biagi R, Fernandez-Rodriguez J, Gonidec M, Mirone A, Corradini V, Moro F, De Renzi V, del Pennino U, Cezar JC, Amabilino DB, Veciana J (2010) Phys Rev B 82:224406
187. Gonidec M, Biagi R, Corradini V, Moro F, De Renzi V, del Pennino U, Summa D, Muccioli L, Zannoni C, Amabilino DB, Veciana J (2011) J Am Chem Soc 133:6603
188. Malavolti L, Poggini L, Margheriti L, Chiappe D, Graziosi P, Cortigiani B, Lanzilotto V, de Mongeot FB, Ohresser P, Otero E, Choueikani F, Sainctavit P, Bergenti I, Dediu VA, Mannini M, Sessoli R (2013) Chem Commun 49:11506
189. Moro F, Biagi R, Corradini V, Evangelisti M, Gambardella A, De Renzi V, del Pennino U, Coronado E, Forment-Aliaga A, Romero FM (2012) J Phys Chem C 116:14936
190. Kahle S, Deng Z, Malinowski N, Tonnoir C, Forment-Aliaga A, Thontasen N, Rinke G, Le D, Turkowski V, Rahman TS, Rauschenbach S, Ternes M, Kern K (2011) Nano Lett 12:518
191. Sun K, Park K, Xie J, Luo J, Yuan H, Xiong Z, Wang J, Xue Q (2013) ACS Nano 7:6825

192. del Pennino U, Corradini V, Biagi R, De Renzi V, Moro F, Boukhvalov DW, Panaccione G, Hochstrasser M, Carbone C, Milios CJ, Brechin EK (2008) Phys Rev B 77:085419
193. Moro F, Corradini V, Evangelisti M, Renzi VD, Biagi R, Pennino UD, Milios CJ, Jones LF, Brechin EK (2008) J Phys Chem B 112:9729
194. Moro F, Corradini V, Evangelisti M, Biagi R, De Renzi V, del Pennino U, Cezar JC, Inglis R, Milios CJ, Brechin EK (2010) Nanoscale 2:2698
195. Cornia A, Mannini M (2014) Single-molecule magnets on surfaces. Struct Bond. doi:10.1007/430_2014_150
196. Mannini M, Pineider F, Danieli C, Totti F, Sorace L, Sainctavit P, Arrio MA, Otero E, Joly L, Cezar JC, Cornia A, Sessoli R (2010) Nature 468:417
197. Scheybal A, Ramsvik T, Bertschinger R, Putero M, Nolting F, Jung TA (2005) Chem Phys Lett 411:214
198. Wende H, Bernien M, Luo J, Sorg C, Ponpandian N, Kurde J, Miguel J, Piantek M, Xu X, Eckhold P, Kuch W, Baberschke K, Panchmatia PM, Sanyal B, Oppeneer PM, Eriksson O (2007) Nat Mater 6:516
199. Bernien M, Miguel J, Weis C, Ali ME, Kurde J, Krumme B, Panchmatia PM, Sanyal B, Piantek M, Srivastava P, Baberschke K, Oppeneer PM, Eriksson O, Kuch W, Wende H (2009) Phys Rev Lett 102:047202
200. Stepanow S, Mugarza A, Ceballos G, Moras P, Cezar JC, Carbone C, Gambardella P (2010) Phys Rev B 82:014405
201. Baker ML, Mutka H (2012) Eur Phys J Spec Top 213:53
202. Amoretti G, Caciuffo R, Carretta S, Guidi T, Magnani N, Santini P (2008) Inorg Chim Acta 361:3771
203. Basler R, Boskovic C, Chaboussant G, Güdel HU, Murrie M, Ochsenbein ST, Sieber A (2003) Chem Phys Chem 4:910
204. Furrer A, Waldmann O (2013) Rev Mod Phys 85:367
205. Squires GL (1996) Introduction to the theory of thermal neutron scattering. Dover, Mineola
206. Marshall W, Lovesey SW (1971) Theory of thermal neutron scattering. Oxford University Press, Oxford
207. Dianoux AJ, Lander G (2003) Neutron data booklet. OCP Science, Grenoble
208. Waldmann O (2003) Phys Rev B 68:174406
209. Caciuffo R, Guidi T, Amoretti G, Carretta S, Liviotti E, Santini P, Mondelli C, Timco G, Muryn CA, Winpenny REP (2005) Phys Rev B 71:174407
210. Russina M, Mezei F (2009) Nucl Instr Meth Phys Res Sect A Accelerators Spectrometers Detectors Assoc Equip 604:624
211. Bewley RI, Taylor JW, Bennington SM (2011) Nucl Instr Meth Phys Res Sect A Accelerators Spectrometers Detectors Assoc Equip 637:128
212. Nakajima K, Ohira-Kawamura S, Kikuchi T, Nakamura M, Kajimoto R, Inamura Y, Takahashi N, Aizawa K, Suzuya K, Shibata K, Nakatani T, Soyama K, Maruyama R, Tanaka H, Kambara W, Iwahashi T, Itoh Y, Osakabe T, Wakimoto S, Kakurai K, Maekawa F, Harada M, Oikawa K, Lechner RE, Mezei F, Arai M (2011) J Phys Soc Jpn 80:SB028
213. Kofu M, Yamamuro O, Kajiwara T, Yoshimura Y, Nakano M, Nakajima K, Ohira-Kawamura S, Kikuchi T, Inamura Y (2013) Phys Rev B 88:064405
214. Furrer A, Güdel HU (1977) Phys Rev Lett 39:657
215. Güdel HU, Furrer A (1977) Mol Phys 33:1335
216. Furrer A, Güdel HU, Blank H, Heidemann A (1989) Phys Rev Lett 62:210
217. Furrer A, Güdel HU, Darriet J (1985) J Less Common Metals 111:223
218. Guedel HU, Furrer A, Blank H (1990) Inorg Chem 29:4081
219. Furrer A, Güdel HU, Krausz ER, Blank H (1990) Phys Rev Lett 64:68
220. Aebersold MA, Güdel HU, Hauser A, Furrer A, Blank H, Kahn R (1993) Phys Rev B 48:12723
221. Sessoli R, Powell AK (2009) Coord Chem Rev 253:2328

222. Rinehart JD, Long JR (2011) Chem Sci 2:2078
223. Caciuffo R, Amoretti G, Murani A, Sessoli R, Caneschi A, Gatteschi D (1998) Phys Rev Lett 81:4744
224. Mirebeau I, Hennion M, Casalta H, Andres H, Güdel HU, Irodova AV, Caneschi A (1999) Phys Rev Lett 83:628
225. Zhong Y, Sarachik MP, Friedman JR, Robinson RA, Kelley TM, Nakotte H, Christianson AC, Trouw F, Aubin SMJ, Hendrickson DN (1999) J Appl Phys 85:5636
226. Ollivier J, Mutka H (2011) J Phys Soc Jpn 80:SB003
227. Cornia A, Fabretti AC, Sessoli R, Sorace L, Gatteschi D, Barra A-L, Daiguebonne C, Roisnel T (2002) Acta Cryst C 58:m371
228. Farrell AR, Coome JA, Probert MR, Goeta AE, Howard JAK, Lemee-Cailleau M-H, Parsons S, Murrie M (2013) Cryst Eng Commun 15:3423
229. Sieber A, Chaboussant G, Bircher R, Boskovic C, Güdel HU, Christou G, Mutka H (2004) Phys Rev B 70:172413
230. Chaboussant G, Sieber A, Ochsenbein S, Güdel HU, Murrie M, Honecker A, Fukushima N, Normand B (2004) Phys Rev B 70:104422
231. Hennion M, Pardi L, Mirebeau I, Suard E, Sessoli R, Caneschi A (1997) Phys Rev B 56:8819
232. Carretta S, Guidi T, Santini P, Amoretti G, Pieper O, Lake B, van Slageren J, Hallak FE, Wernsdorfer W, Mutka H, Russina M, Milios CJ, Brechin EK (2008) Phys Rev Lett 100:157203
233. Pieper O, Guidi T, Carretta S, van Slageren J, El Hallak F, Lake B, Santini P, Amoretti G, Mutka H, Koza M, Russina M, Schnegg A, Milios CJ, Brechin EK, Julià A, Tejada J (2010) Phys Rev B 81:174420
234. Garlea VO, Nagler SE, Zarestky JL, Stassis C, Vaknin D, Kögerler P, McMorrow DF, Niedermayer C, Tennant DA, Lake B, Qiu Y, Exler M, Schnack J, Luban M (2006) Phys Rev B 73:024414
235. Schnack J (2010) Dalton Trans 39:4677
236. Baker ML, Timco GA, Piligkos S, Mathieson JS, Mutka H, Tuna F, Kozłowski P, Antkowiak M, Guidi T, Gupta T, Rath H, Woolfson RJ, Kamieniarz G, Pritchard RG, Weihe H, Cronin L, Rajaraman G, Collison D, McInnes EJL, Winpenny REP (2012) Proc Natl Acad Sci 109:19113
237. Iida K, Qiu Y, Sato TJ (2011) Phys Rev B 84:094449
238. Kögerler P, Tsukerblat B, Möller A (2010) Dalton Trans 39:21
239. Affronte M, Carretta S, Timco GA, Winpenny REP (2007) Chem Commun 2007:1789
240. Steiner M, Tennant DA, Smeibidl P (2006) J Phys Conf Ser 51:470
241. Müller A, Döring J (1988) Angew Chem Int Ed 27:1721
242. Mourigal M, Fuhrman WT, Sheckelton JP, Wartelle A, Rodriguez-Rivera JA, Abernathy DL, McQueen TM, Broholm CL (2014) Phys Rev Lett 112:027202
243. Barra AL, Gatteschi D, Pardi L, Mueller A, Doering J (1992) J Am Chem Soc 114:8509
244. Gatteschi D, Pardi L, Barra AL, Muller A, Doring J (1991) Nature 354:463
245. Chiorescu I, Wernsdorfer W, Müller A, Bögge H, Barbara B (2000) Phys Rev Lett 84:3454
246. Chaboussant G, Basler R, Sieber A, Ochsenbein ST, Desmedt A, Lechner RE, Telling MTF, Kögerler P, Müller A, Güdel HU (2002) Europhys Lett 59:291
247. Chaboussant G, Ochsenbein ST, Sieber A, Güdel H-U, Mutka H, Müller A, Barbara B (2004) Europhys Lett 66:423
248. Carretta S, Santini P, Amoretti G, Guidi T, Copley JRD, Qiu Y, Caciuffo R, Timco G, Winpenny REP (2007) Phys Rev Lett 98:167401
249. Waldmann O, Carver G, Dobe C, Biner D, Sieber A, Güdel HU, Mutka H, Ollivier J, Chakov NE (2006) Appl Phys Lett 88:042507
250. Waldmann O, Carver G, Dobe C, Sieber A, Güdel HU, Mutka H (2007) J Am Chem Soc 129:1526
251. Chiolero A, Loss D (1998) Phys Rev Lett 80:169
252. Normand B, Wang X, Zotos X, Loss D (2001) Phys Rev B 63:184409

253. Bärwinkel K, Hage P, Schmidt H-J, Schnack J (2003) Phys Rev B 68:054422
254. Bärwinkel K, Schmidt HJ, Schnack J (2000) J Magn Magn Mater 212:240
255. Timco GA, McInnes EJL, Winpenny REP (2013) Chem Soc Rev 42:1796
256. Waldmann O, Guidi T, Carretta S, Mondelli C, Dearden AL (2003) Phys Rev Lett 91:237202
257. Dreiser J, Waldmann O, Dobe C, Carver G, Ochsenbein ST, Sieber A, Güdel HU, van Duijn J, Taylor J, Podlesnyak A (2010) Phys Rev B 81:024408
258. Ummethum J, Nehrkorn J, Mukherjee S, Ivanov NB, Stuiber S, Strässle T, Tregenna-Piggott PLW, Mutka H, Christou G, Waldmann O, Schnack J (2012) Phys Rev B 86:104403
259. Baker ML, Waldmann O, Piligkos S, Bircher R, Cador O, Carretta S, Collison D, Fernandez-Alonso F, McInnes EJL, Mutka H, Podlesnyak A, Tuna F, Ochsenbein S, Sessoli R, Sieber A, Timco GA, Weihe H, Güdel HU, Winpenny REP (2012) Phys Rev B 86:064405
260. Waldmann O, Stamatatos TC, Christou G, Güdel HU, Sheikin I, Mutka H (2009) Phys Rev Lett 102:157202
261. Waldmann O, Dobe C, Mutka H, Furrer A, Güdel HU (2005) Phys Rev Lett 95:057202
262. Furukawa Y, Kiuchi K, Kumagai K-I, Ajiro Y, Narumi Y, Iwaki M, Kindo K, Bianchi A, Carretta S, Timco GA, Winpenny REP (2008) Phys Rev B 78:092402
263. Taft KL, Delfs CD, Papaefthymiou GC, Foner S, Gatteschi D, Lippard SJ (1994) J Am Chem Soc 116:823
264. Honecker A, Meier F, Loss D, Normand B (2002) Eur Phys J B 27:487
265. Carretta S, van Slageren J, Guidi T, Liviotti E, Mondelli C, Rovai D, Cornia A, Dearden AL, Carsughi F, Affronte M, Frost CD, Winpenny REP, Gatteschi D, Amoretti G, Caciuffo R (2003) Phys Rev B 67:094405
266. Bianchi A, Carretta S, Santini P, Amoretti G, Guidi T, Qiu Y, Copley JRD, Timco G, Muryn C, Winpenny REP (2009) Phys Rev B 79:144422
267. Santini P, Carretta S, Amoretti G, Guidi T, Caciuffo R, Caneschi A, Rovai D, Qiu Y, Copley JRD (2005) Phys Rev B 71:184405
268. Waldmann O, Bircher R, Carver G, Sieber A, Güdel HU, Mutka H (2007) Phys Rev B 75:174438
269. Ehlers G, Podlesnyak AA, Niedziela JL, Iverson EB, Sokol PE (2011) Rev Sci Instrum 82:085108
270. Baker ML, Guidi T, Carretta S, Ollivier J, Mutka H, Gudel HU, Timco GA, McInnes EJL, Amoretti G, Winpenny REP, Santini P (2012) Nat Phys 8:906
271. Perring TG, Ewings RA, Duijn JV Visualising and manipulating $S(\boldsymbol{q}, \omega)$ measured in all four dimensions (unpublished). http://horace.isis.rl.ac.uk
272. Zyazin AS, van den Berg JWG, Osorio EA, van der Zant HSJ, Konstantinidis NP, Leijnse M, Wegewijs MR, May F, Hofstetter W, Danieli C, Cornia A (2010) Nano Lett 10:3307
273. del Carmen Giménez-López M, Moro F, La Torre A, Gómez-García CJ, Brown PD, van Slageren J, Khlobystov AN (2011) Nat Commun 2:407
274. Wernsdorfer W, Aliaga-Alcalde N, Hendrickson DN, Christou G (2002) Nature 416:406
275. Timco GA, Carretta S, Troiani F, Tuna F, Pritchard RJ, Muryn CA, McInnes EJL, Ghirri A, Candini A, Santini P, Amoretti G, Affronte M, Winpenny REP (2009) Nat Nanotechnol 4:173
276. Luzon J, Bernot K, Hewitt IJ, Anson CE, Powell AK, Sessoli R (2008) Phys Rev Lett 100:247205
277. Cador O, Gatteschi D, Sessoli R, Larsen FK, Overgaard J, Barra A-L, Teat SJ, Timco GA, Winpenny REP (2004) Angew Chem Int Ed 43:5196
278. Lindroos M, Bousson S, Calaga R, Danared H, Devanz G, Duperrier R, Eguia J, Eshraqi M, Gammino S, Hahn H, Jansson A, Oyon C, Pape-Møller S, Peggs S, Ponton A, Rathsman K, Ruber R, Satogata T, Trahern G (2011) Nucl Instr Meth Phys Res Sect B Beam Interact Mater Atoms 269:3258
279. Blundell SJ (1999) Contemp Phys 40:175
280. Blundell SJ (2004) Chem Rev 104:5717
281. Lancaster T, Blundell SJ, Brooks ML, Baker PJ, Pratt FL, Manson JL, Landee CP, Baines C (2006) Phys Rev B 73, R020410

282. Lancaster T, Blundell SJ, Pratt FL (2013) Phys Scr 88:068506
283. Blundell SJ, Lancaster T, Pratt FL, Baker PJ, Brooks ML, Baines C, Manson JL, Landee CP (2007) J Phys Chem Solids 68:2039
284. Sengupta P, Sandvik AW, Singh RRP (2003) Phys Rev B 68:094423
285. Lascialfari A, Jang ZH, Borsa F, Carretta P, Gatteschi D (1998) Phys Rev Lett 81:3773
286. Salman Z, Keren A, Mendels P, Marvaud V, Scuiller A, Verdaguer M, Lord JS, Baines C (2002) Phys Rev B 65:132403
287. Blundell SJ, Pratt FL, Marshall IM, Steer CA, Hayes W, Letard JF, Heath SL, Caneschi A, Gatteschi D (2003) Synth Met 133–134:531
288. Lancaster T, Blundell SJ, Pratt FL, Brooks ML, Manson JL, Brechin EK, Cadiou C, Low D, McInnes EJL, Winpenny REP (2004) J Phys Condens Matter 16:S4563
289. Salman Z, Kiefl RF, Chow KH, MacFarlane WA, Keeler TA, Parolin TJ, Tabbara S, Wang D (2008) Phys Rev B 77:214415
290. Keren A, Shafir O, Shimshoni E, Marvaud V, Bachschmidt A, Long J (2007) Phys Rev Lett 98:257204
291. Lancaster T, Blundell SJ, Pratt FL, Franke I, Steele AJ, Baker PJ, Salman Z, Baines C, Watanabe I, Carretta S, Timco GA, Winpenny REP (2010) Phys Rev B 81:140409(R)
292. Larsen FK, McInnes EJL, El Mkami H, Overgaard J, Piligkos S, Rajaraman G, Rentschler E, Smith AA, Smith GM, Boote V, Jennings M, Timco GA, Winpenny REP (2003) Angew Chem Int Ed 42:101
293. van Slageren J, McInnes EJL, El Mkami H, Overgaard J, Piligkos S, Rajaraman G, Rentschler E, Smith AA, Smith GM, Boote V, Jennings M, Timco GA, Winpenny REP (2002) Chem Eur J 8:277
294. Hayano RS, Uemura YJ, Imazato J, Nishida N, Yamazaki T, Kubo R (1979) Phys Rev B 20:850
295. Lancaster T, Möller JS, Blundell SJ, Pratt FL, Baker PJ, Guidi T, Timco GA, Winpenny REP (2011) J Phys Condens Matter 23:242201
296. Salman Z, Blundell SJ (2012) Phys Proc 30:168
297. Hofmann A, Salman Z, Mannini M, Amato A, Malavolti L, Morenzoni E, Prokscha T, Sessoli R, Suter A (2012) ACS Nano 6:8390